SIAM J. SCI. COMPUT.
Vol. 46, No. 1, pp. A23–A49

ON OPTIMAL ZERO-PADDING OF KERNEL TRUNCATION METHOD*

XIN LIU†, QINGLIN TANG‡, SHAOBO ZHANG§, AND YONG ZHANG†

Abstract. The kernel truncation method (KTM) is a commonly used algorithm to compute the convolution-type nonlocal potential $\Phi(\mathbf{x}) = (U * \rho)(\mathbf{x})$, $\mathbf{x} \in \mathbb{R}^d$, where the convolution kernel $U(\mathbf{x})$ might be singular at the origin and/or far-field and the density $\rho(\mathbf{x})$ is smooth and fast decaying. In KTM, in order to capture the Fourier integrand's oscillations that are brought by the kernel truncation, one needs to carry out a zero-padding of the density, which means a larger physical computation domain and a finer mesh in the Fourier space by duality. The zero-padding factor, $\sqrt{d}+1$, was first given as empirical formula for the 2D/3D Coulomb potential in [M. R. Jarvis et al. *Phys. Rev. B,* 56 (1997), pp. 14972–14978; C. A. Rozzi et al. *Phys. Rev. B,* 73 (2006), 205119]. In this article, we first rederive the optimal zero-padding factor in a rigorous way for arbitrary space dimension and different nonlocal potentials. Then, we present the error estimates of the density and potential. Next, we investigate the anisotropic density case, and provide details of tensor acceleration [F. Vico, L. Greengard, and M. Ferrando, *J. Comput. Phys.* 323 (2016), pp. 191–203], which is an important performance improvement. Finally, extensive numerical results are provided to confirm the accuracy, efficiency, optimal zero-padding factor for the anisotropic density, together with some applications to different nonlocal potentials, including the one-dimensional/two-dimensional (2D)/three-dimensional (3D) Poisson, 2D Coulomb, quasi-2D/3D dipole-dipole Interaction, and 3D quadrupolar potential.

Key words. convolution-type nonlocal potential, kernel truncation method, optimal zero-padding, error estimates, anisotropic density

MSC codes. 65D32, 68Q25

DOI. 10.1137/23M1550803

1. Introduction.

In the science and engineering community, nonlocal potentials, which are given by a convolution of a translational invariant Green's function with a fast-decaying smooth function, are quite universal and common, e.g., the Newtonian potential in cosmology, the Poisson potential in electrostatics, plasma physics and quantum physics, and are often used to account for long-range interaction. In this article, we consider the following convolution-type nonlocal potential

$$\Phi(\mathbf{x}) = [U * \rho](\mathbf{x}) = \int_{\mathbb{R}^d} U(\mathbf{x}-\mathbf{y})\rho(\mathbf{y})\mathrm{d}\mathbf{y}, \quad \mathbf{x} \in \mathbb{R}^d, \tag{1.1}$$

*Submitted to the journal's Numerical Algorithms for Scientific Computing section February 1, 2023; accepted for publication (in revised form) June 28, 2023; published electronically January 10, 2024.

https://doi.org/10.1137/23M1550803

Funding: The work of the second author was supported by the National Natural Science Foundation of China grant 11971335 and by the Institutional Research Fund from Sichuan University grant 2020SCUNL110. The work of the first, third, and fourth authors was supported by the National Natural Science Foundation of China grant 12271400 and by Tianyuan Mathematical Center in Southwest China grant 12226102.

†Center for Applied Mathematics, Tianjin University, Tianjin, 300072, China (liuxin_921@tju.edu.cn, Zhang_Yong@tju.edu.cn).

‡School of Mathematics, SiChuan University, ChengDu, 610065, China (qinglin_tang@scu.edu.cn).

§Corresponding author. Center for Applied Mathematics, Tianjin University, Tianjin, 300072, China (shaobo_zhang@tju.edu.cn).

where $*$ is the convolution operator, $\mathbf{x} = (x_1, \ldots, x_d) \in \mathbb{R}^d$, $d = 1, 2, 3$, is the spatial dimension. The potential can also be rewritten in Fourier integral form,

$$\Phi(\mathbf{x}) = \frac{1}{(2\pi)^d} \int_{\mathbb{R}^d} \widehat{U}(\mathbf{k}) \widehat{\rho}(\mathbf{k}) e^{i\mathbf{k}\cdot\mathbf{x}} \mathrm{d}\mathbf{k}, \quad \mathbf{x} \in \mathbb{R}^{\mathrm{d}}, \tag{1.2}$$

where $\widehat{f}(\mathbf{k}) = \int_{\mathbb{R}^d} f(\mathbf{x}) e^{-i\mathbf{k}\cdot\mathbf{x}} \mathrm{d}\mathbf{x}$ is the Fourier transform of function $f(\mathbf{x})$. The density $\rho(\mathbf{x})$ is a fast-decaying smooth function and the convolution kernel $U(\mathbf{x})$ is usually singular at the origin and/or at the far field. The Fourier transform of convolution kernel $\widehat{U}(\mathbf{k})$ is singular too, and sometimes the singularity becomes even stronger, e.g., the two-dimensional (2D) Poisson kernel $-\frac{1}{2\pi} \ln(|\mathbf{x}|)$.

Since the density decays fast enough, it is reasonable to assume that the density is numerically compactly supported in a bounded domain $\Omega \subset \mathbb{R}^d$, that is, $\mathrm{supp}\{\rho\} \subset \Omega$. In computational practice, we first truncate the whole space into a rectangular domain, i.e., $\prod_{j=1}^d [-L_j, L_j]$, and discretize it by $N_j \in 2\mathbb{Z}^+$ equally spaced points in the jth direction. The uniform mesh grid set is denoted as

$$\mathcal{T} := \left\{ (x_1, x_2, \ldots, x_d) \,\middle|\, x_j \in \left\{ \frac{2L_j}{N_j} \ell,\ \ell = -\frac{N_j}{2}, \cdots, \frac{N_j}{2} - 1 \right\},\ j = 1, \ldots, d. \right\} \tag{1.3}$$

The numerical problem is to compute the potential Φ on the grid set $\mathcal{T}$, with discrete density values given on the same grid set, that is,

$$\big\{\rho(\mathbf{x}_i)\big\} \longmapsto \big\{\Phi(\mathbf{x}_i)\big\}. \tag{1.4}$$

As is well known, the density function $\rho(\mathbf{x})$ is well approximated by the Fourier spectral method with spectral accuracy, and it is implemented by the discrete fast Fourier transform (FFT) [19, 20]. It is clear that direct discretization of either (1.1) or (1.2) shall encounter the singularity because the source and target grid coincide; therefore, it requires special care to deal with the singularity in order to guarantee accuracy. During the last ten years, there have been several fast spectral methods developed based on the Fourier spectral method, such as the nonuniform FFT method (NUFFT) [13], the Gaussian-summation method (GauSum) [10], the kernel truncation method (KTM) [21], and the anisotropic truncated kernel method (ATKM) [11], where the singularity is suitably treated with a windowed function or kernel truncation technique in physical/Fourier space. All these methods are spectrally accurate and efficient with an $\mathcal{O}(N_{\mathrm{t}} \log(N_{\mathrm{t}}))$ complexity, where $N_{\mathrm{t}} := \prod_{j=1}^d N_j$ is the total number of grid points. Among them, KTM is the simplest one and has been widely adopted by the physics community to compute the nonlocal potentials [16, 17].

To compute the potential $\Phi(\mathbf{x})$ inside domain Ω, the very basic idea of KTM is to screen unnecessary interactions at the faraway distance, which leads to an effective truncated kernel $U_D(\mathbf{x}) = U(\mathbf{x}) \chi_D(\mathbf{x})$ with $\chi_D(\mathbf{x})$ being the characteristic function of domain D, and then to compute the new convolution $(U_D * \rho)$ since it coincides with the original potential inside the domain of interest, i.e.,

$$\Phi(\mathbf{x}) = [U_D * \rho](\mathbf{x}) \quad \forall\, \mathbf{x} \in \Omega. \tag{1.5}$$

In KTM, we choose to cut off interactions outside a large circular domain $D \subset \mathbb{R}^d$ by simply setting it to zero, i.e., $U(\mathbf{x}) = 0$ for $\mathbf{x} \notin D$; then we apply the trapezoidal rule to the resulting Fourier integral

$$\Phi(\mathbf{x}) = \frac{1}{(2\pi)^d} \int_{\mathbb{R}^d} \widehat{U}_D(\mathbf{k})\ \widehat{\rho}(\mathbf{k})\ e^{i\mathbf{k}\cdot\mathbf{x}}\ \mathrm{d}\mathbf{k}, \quad \mathbf{x} \in \Omega, \tag{1.6}$$

where the Fourier integrand is smooth but oscillatory due to the Paley–Wiener theorem [18]. To resolve the unpleasant oscillations caused by the kernel truncation, it requires a fine mesh in the Fourier space or, equivalently a larger physical domain.

The most natural way is to extend the density to a larger domain $\widetilde{\Omega} = \prod_{j=1}^{d}[-SL_j, SL_j]$ by zero padding, that is, setting $\rho(\mathbf{x}) = 0, \forall \mathbf{x} \in \widetilde{\Omega} \setminus \Omega$. The constant $S > 1$ is called the zero-padding factor hereafter. By duality, the Fourier mesh size is scaled down by a factor of $1/S$, and it helps to provide a better approximation so as to capture the integrand's oscillations. On the other hand, larger extension requires more storage and computational efforts and it inevitably results in a poorer performance. Therefore, the *optimal* zero-padding factor, which is both *necessary* and *sufficient*, is of significant importance to achieve better accuracy with the most economic efforts, especially in high dimension.

The zero-padding factor $S = \sqrt{d}+1$ was first proposed as an empirical formula for the 2D/three-dimensional (3D) Coulomb potential in [12, 17]. However, there has been little literature that ever provides a clear or rigorous explanation for its optimality so far. Another important result, given by Vico, Greengard, and Ferrando in [21], pointed out that a *fourfold* zero-padding is sufficient for machine-precision accuracy. With such fourfold padding, a typical double-precision computation on 256^3 grid shall require a minimum 8 Gb just to store the padded density, not to mention the auxiliary variables whose size is usually even larger; therefore, potential evaluation of such a size or any larger size seems to be an impossible task on limited-memory architecture, such as a personal computer. Fortunately, using a similar periodicity argument as in ATKM [11], we can prove strictly that $S_{\text{opt}} = \sqrt{d}+1$ is the optimal zero-padding factor for any d space dimensions and different nonlocal potentials. For isotropic density, compared with fourfold zero-padding, the optimal zero-padding factor helps reduce the memory costs by a factor of $1-(\frac{\sqrt{3}+1}{4})^3$ in 3D, and alleviate the heavy burden on computational costs greatly. In practice, a threefold (ceiling up of $\sqrt{3}+1$ to its nearest integer), instead of fourfold, zero-padding is adopted to guarantee machine-precision accuracy of nonlocal potentials, which immediately helps reduce memory costs by a factor around 60%, and thus makes the laptop computation possible.

Numerically, the Fourier integral (1.6) is discretized by applying the trapezoidal rule on a uniform mesh grid, and the resulting summation is accelerated by FFT/iFFT (inverse FFT). As pointed out in [21], the trapezoidal rule boils down to a discrete convolution with discrete density of length N_{t}, and such discrete convolution can be accelerated by FFT on a doubly padded density. The convolution tensor T, an accurate approximation of the interaction kernel, is determined by taking an inverse discrete Fourier transform on the truncated kernel's Fourier transform, and its analytical expression is explicitly given by (2.26) in section 2.2. Once the convolution tensor T is available, the potential is computed with a pair of FFT/iFFT on a double-sized vector of length $2^d N_{\text{t}}$.

Another important situation is the anisotropic density case where ρ is (numerically) compactly supported in an anisotropic domain. The KTM applies readily with ease, but the memory requirement and computational costs both scale linearly with the anisotropy strength, which makes it prohibitively expensive for strongly anisotropic density especially in high dimensions. Similar to the isotropic case, the discrete nonlocal potential for anisotropic density can also be written as a discrete convolution that only involves discrete density values. In simulation, the potentials are usually called multiple times with the same numerical setups, for example, in the computation of ground state and dynamics of the nonlocal Schrödinger equation [3, 5, 8]; then

it is worth the efforts to precompute any possible quantities once and for all for the sake of efficiency. Once the convolution tensor is available via a precomputation step, the effective computation is merely a FFT and iFFT pair on a double-sized density regardless of the anisotropy strength, which is of significant importance in practice.

The paper is organized as follows. In section 2, first, we derive and prove the optimal zero-padding of the density in one-dimension (1D)/2D/3D. Then, we reinvestigate the anisotropic density case. Third, we present the discrete convolution structure for isotropic and anisotropic cases, together with an explicit formulation of the convolution tensor and a doubly FFT acceleration in subsection 2.2. Last, we give rigorous error estimates for both the nonlocal potential in subsection 2.3 and the density in Appendix A. Extensive numerical results are shown in section 3 to illustrate the performance of our method in terms of accuracy and efficiency. Finally, some conclusions are drawn in section 4.

2. The optimal zero-padding. In this section, we first focus on computation of the nonlocal potential generated by isotropic density, and discuss the anisotropic case later. For simplicity, we choose a square domain, i.e., $\mathbf{R}_L = \prod_{j=1}^{d}[-L, L]$, which is discretized with N equally spaced grid points in each spatial direction, and denote the mesh grid (1.3) as $\mathcal{T}_N$. The density $\rho(\mathbf{x})$ is well approximated by the Fourier spectral method inside $\mathbf{R}_L$ [19, 20].

The nonlocal potential (1.1) can be reformulated as follows:

$$\Phi(\mathbf{x}) = \int_{\mathbb{R}^d} U(\mathbf{x}-\mathbf{y})\rho(\mathbf{y})\ \mathrm{d}\mathbf{y} = \int_{\mathbf{R}_L} U(\mathbf{x}-\mathbf{y})\rho(\mathbf{y})\mathrm{d}\mathbf{y} \tag{2.1}$$

$$= \int_{\mathbf{x}+\mathbf{R}_L} U(\mathbf{y})\rho(\mathbf{x}-\mathbf{y})\mathrm{d}\mathbf{y}. \tag{2.2}$$

As the density is compactly supported in $\mathbf{R}_L$, (2.2) is equivalent to the following convolution,

$$\Phi(\mathbf{x}) = \int_{\mathbf{B}_G} U(\mathbf{y})\rho(\mathbf{x}-\mathbf{y})\mathrm{d}\mathbf{y}, \qquad \mathbf{x}\in\mathbf{R}_L, \tag{2.3}$$

where $\mathbf{B}_G$ is a ball centered at the origin with radius $G := \max_{\mathbf{x},\mathbf{y}\in\mathbf{R}_L}|\mathbf{x}-\mathbf{y}| = 2\sqrt{d}L$ being the diameter of $\mathbf{R}_L$. The above equation holds because, for any $\mathbf{x}\in\mathbf{R}_L$, $\mathbf{y}\in\mathbf{B}_G\backslash(\mathbf{x}+\mathbf{R}_L)$, we have

$$\mathbf{x}-\mathbf{y}\notin\mathbf{R}_L \ \longrightarrow\ \rho(\mathbf{x}-\mathbf{y})=0 \ \Longrightarrow\ \int_{\mathbf{B}_G\backslash(\mathbf{x}+\mathbf{R}_L)} U(\mathbf{y})\rho(\mathbf{x}-\mathbf{y})\mathrm{d}\mathbf{y}=0. \tag{2.4}$$

To integrate (2.3), one needs to approximate the density $\rho(\mathbf{x})$ on a domain $\mathbf{R}_{\text{ess}} := \mathbf{R}_{(2\sqrt{d}+1)L}$, which we rename as the essential domain for presentation's convenience, because, for any $\mathbf{x}\in\mathbf{R}_L$ and $\mathbf{y}\in\mathbf{B}_G$, we have

$$\mathbf{x}-\mathbf{y}\in\mathbf{R}_{(2\sqrt{d}+1)L}. \tag{2.5}$$

It is worth pointing out that spectral approximation of the density in any larger or smaller domain than $\mathbf{R}_{\text{ess}}$ shall result in efficiency degeneration or accuracy lost. In other words, it is both sufficient and necessary to require a spectral approximation of the density within $\mathbf{R}_{\text{ess}}$.

To approximate $\rho(\mathbf{x})$ within the essential domain, it is natural to extend the density to $\mathbf{R}_{\text{ess}}$ by zero-padding and apply the Fourier spectral method therein. With

such plain extension, one shall zero-pad the density in each spatial direction by a factor of $2\sqrt{d}+1$, and the corresponding memory cost is $(2\sqrt{d}+1)^d$ times that for the original density discretization, which amounts to a huge memory requirement 88 times larger in 3D. As pointed out in [21], a fourfold zero-padding is sufficient for machine-precision accuracy in 3D, therefore, we conclude that this is actually not the most economic way. In fact, by utilizing periodicity of Fourier series, we will see later that the zero-padding factor could be reduced to $\sqrt{d}+1$, which significantly alleviates the memory/computational costs. It is important to remark here that such a zero-padding factor guarantees a spectral approximation of the density within $\mathbf{R}_{\text{ess}}$.

It is well known that the Fourier series can be simultaneously extended periodically over the whole space $\mathbb{R}^d$. Therefore, the zero-padded domain $\mathbf{R}_{SL}$ does not necessarily need to cover the concerned domain directly, and it can be selected as a smaller domain, i.e., $S < 2\sqrt{d}+1$. The minimum zero-padding factor to guarantee full accuracy is named optimal zero-padding factor S_{opt}. Making full use of Fourier series' periodicity and whole space extension, we derive the optimal zero-padding factor as follows.

THEOREM 1. *To compute the d-dimensional convolution-type nonlocal potential* (1.1) *using the KTM* [21]*, there exists an optimal zero-padding factor, i.e.,* $S_{\text{opt}} = \sqrt{d}+1$*, and it helps achieve machine-precision in the potential with the smallest memory costs.*

Proof. Let us assume that the density function $\rho(\mathbf{x})$ is approximated by a finite Fourier series within the S-fold zero-padded domain $\mathbf{R}_{SL}$. Due to the Fourier series' periodicity, the Fourier series extends naturally over the whole space. It is not difficult to find that such Fourier series guarantee a spectral approximation of $\rho(\mathbf{x})$ within $(2S-1)$-fold domain $\mathbf{R}_{(2S-1)L}$. In fact, as long as $\mathbf{R}_{(2\sqrt{d}+1)L} \subseteq \mathbf{R}_{(2S-1)L}$ holds true, the Fourier series suffices as a machine-precision approximation of the density within the concerned domain $\mathbf{R}_{(2\sqrt{d}+1)L}$.

Equivalently, once the following inequality

$$2\sqrt{d}+1 \le 2S-1 \Longleftrightarrow \sqrt{d}+1 \le S \tag{2.6}$$

is satisfied, the S-fold zero-padding is both sufficient and necessary, and the optimal zero-padding factor S_{opt} is chosen as the one when the equality holds, that is,

$$S_{\text{opt}} = \sqrt{d}+1. \tag{2.7}$$

In practice, it is convenient to choose

$$S_{\text{opt}} = \lceil \sqrt{d}+1 \rceil, \tag{2.8}$$

where $\lceil\ \rceil$ is rounding up to the nearest integer. Numerically, S_{opt} is 2 in 1D and 3 for the 2D and 3D problems.

To make the above argument clearer, we present a 1D graphical illustration of the twofold (left) and threefold (right) zero-padding of the density (blue solid line) and the periodic extensions (green dashed line) in Figure 1. It is quite clear that the periodic extension of a twofold zero-padding coincides with the density within $\mathbf{R}_{(2\times 2-1)L} = \mathbf{R}_{3L}$; while, without zero-padding, periodic extension of the Fourier series approximation, that is done over the original domain $\mathbf{R}_L$, mismatches the density $\rho(\mathbf{x})$ in $[L, 3L]$ with a nonnegligible error. Therefore, we conclude that a twofold zero-padding suffices to guarantee a spectral approximation in 1D. The same argument

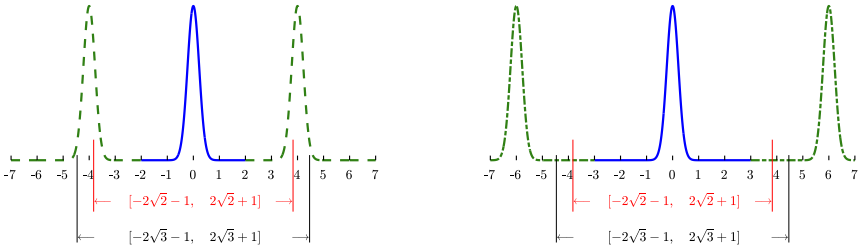

FIG. 1. *Periodic extensions of the twofold (left) and threefold (right) zero-padding for the density. Here* $L = 1$ *for simplicity.*

applies to the other spatial direction, therefore, without difficulty, we can see that threefold zero-padding suffices for spectral approximation in the 2D and 3D cases. ∎

Remark 2.1. The periodic extension holds in each spatial dimension, therefore, arguments of the optimal zero-padding apply to more general rectangular domains and different grid point numbers, that is, the spatial extend $[-L_j, L_j]$ and grid number N_j along the jth spatial direction are not necessarily the same.

Remark 2.2. In practice, for sake of an even better efficiency, we can also consider a fractional zero-padding, e.g., $S = \frac{5}{2}$, as long as $N_j S \in 2\mathbb{Z}^+$ with $j = 1, 2, 3$. Taking the 2D case as an example, the analytical optimal zero-padding factor $\sqrt{2}+1 \approx 2.4$ is close to 2.5 but smaller than $\lceil\sqrt{2}+1\rceil = 3$, we may choose a 2.5-fold zero-padding for smaller memory costs and better efficiency.

Remark 2.3. In standard KTM [17, 21], one chooses to integrate the corresponding Fourier integral of (2.3) by applying the trapezoidal rule quadrature, but it was not clear how to choose the optimal mesh size so as to capture the integrand's oscillations. For the first time, we derive the optimal zero-padding factor and point out that the typical fourfold zero-padding is only sufficient but not necessary. The optimal zero-padding factor (2.7) helps reduce the memory costs by a factor $1 - (\frac{S_{\text{opt}}}{4})^d$, and the memory reduction is quite significant in higher space dimensions. For example, in the precomputation step of (2.14), a double-precision computation on a 256^3 grid requires a minimum of 3.4 Gb memory with the optimal threefold zero-padding while the fourfold original algorithm requires around 8 Gb, with the reduction factor being around 60%.

Remark 2.4. The isotropic kernel truncation facilitates the computation of the corresponding Fourier transform, which is exactly what the classical KTM adopted [17, 21]. It is worthy to point out that the isotropic kernel truncation is not optimal in terms of efficiency, simply because the geometry of the computation domain is not taken into account. Anisotropic kernel extension to a larger rectangular domain produces better efficiency, and we refer the readers to [11] for more details.

On domain $\mathbf{R}_{SL}$, the density ρ is well resolved by the following finite Fourier series

$$\rho(\mathbf{z}) \approx \sum_{\mathbf{k}\in\Lambda} \widehat{\rho}_{\mathbf{k}}\, e^{i\mathbf{k}\cdot\mathbf{z}}, \qquad \mathbf{z} \in \mathbf{R}_{SL}, \tag{2.9}$$

where $\Lambda = \{\mathbf{k} := \frac{\pi}{SL}(k_1, \ldots, k_d) \in \frac{\pi}{SL}\mathbb{Z}^d \ \ \big| k_j = -\frac{SN}{2}, \ldots, \frac{SN}{2} - 1, j = 1, \ldots, d\}$ is the mesh grid in Fourier space. The Fourier coefficients are given as follows:

$$\widehat{\rho}_{\mathbf{k}} = \frac{1}{(2SL)^d} \int_{\mathbf{R}_{SL}} \rho(\mathbf{z}) e^{-i\mathbf{k}\cdot\mathbf{z}} \mathrm{d}\mathbf{z}, \qquad \mathbf{k} \in \Lambda. \tag{2.10}$$

Such an integral is well approximated by applying the trapezoidal rule, and the resulting summation, which is given explicitly as follows,

$$\widetilde{\rho}_{\mathbf{k}} = \frac{1}{(SN)^d} \sum_{\mathbf{z_p} \in \mathcal{T}_{SN}} \rho(\mathbf{z_p}) e^{-i\mathbf{z_p}\cdot\mathbf{k}}, \quad \mathbf{k} \in \Lambda, \tag{2.11}$$

is accelerated by discrete FFT within $\mathcal{O}(d(SN)^d \log(SN))$ float operations [19, 20]. Then we obtain the following finite Fourier series,

$$\rho_N(\mathbf{z}) := \sum_{\mathbf{k}\in\Lambda} \widetilde{\rho}_{\mathbf{k}}\ e^{i\mathbf{k}\cdot\mathbf{z}}, \quad \mathbf{z} \in \mathbf{R}_{SL}, \tag{2.12}$$

which is an interpolation on $\mathcal{T}_{SN}$ and a spectral approximation of $\rho(\mathbf{x})$ over $\mathbf{R}_{SL}$. As is shown earlier, the periodic extension of $\rho_N(\mathbf{z})$ is also a spectral approximation over $\mathbf{R}_{(2\sqrt{d}+1)L}$; therefore, after substituting ρ_N for ρ in (2.3), we obtain

$$\begin{aligned} \Phi(\mathbf{x}) &\approx \int_{\mathbf{B}_G} U(\mathbf{y}) \rho_N(\mathbf{x}-\mathbf{y}) \mathrm{d}\mathbf{y}, \\ &= \sum_{\mathbf{k}\in\Lambda} \left(\int_{\mathbf{B}_G} U(\mathbf{y}) e^{-i\mathbf{k}\cdot\mathbf{y}} \mathrm{d}\mathbf{y} \right) \widetilde{\rho}_{\mathbf{k}}\ e^{i\mathbf{k}\cdot\mathbf{x}}, \\ &:= \sum_{\mathbf{k}\in\Lambda} \widehat{U_G}(\mathbf{k})\ \widetilde{\rho}_{\mathbf{k}}\ e^{i\mathbf{k}\cdot\mathbf{x}} := \Phi_N(\mathbf{x}), \quad \mathbf{x} \in \mathbf{R}_L, \end{aligned} \tag{2.13}$$

where $\widehat{U_G}(\mathbf{k})$, Fourier transform of the truncated kernel, is defined as

$$\widehat{U_G}(\mathbf{k}) := \int_{\mathbf{B}_G} U(\mathbf{y})\ e^{-i\mathbf{k}\cdot\mathbf{y}} \mathrm{d}\mathbf{y}. \tag{2.14}$$

The above approximation of Φ is spectrally accurate, and its evaluation on target grid $\mathcal{T}_N$ is accelerated by FFT with great efficiency.

The truncated kernel's Fourier transform is computed once and for all and can be treated as a precomputation. For symmetric kernels, i.e., $U(\mathbf{x}) = U(r)$ with $r = |\mathbf{x}|$, the Fourier transform will be reduced to a 1D integral as follows [21],

$$\widehat{U_G}(\mathbf{k}) = \begin{cases} 2\pi \int_0^G J_0(kr) U(r) r\ \mathrm{d}r, & d = 2, \\ 4\pi \int_0^G \frac{\sin(kr)}{kr} U(r) r^2\ \mathrm{d}r, & d = 3, \end{cases} \tag{2.15}$$

where J_0 is the Bessel function of first kind with index 0. For the most common classical kernels, e.g., the Poisson and Coulomb kernels, (2.15) has analytical expressions and we refer to [3, 21] for more details. For general kernels, one may resort to numerical integration, e.g., the Gauss–Kronrod quadrature [3], or some high-precision libraries such as the Advanpix toolbox [1], to obtain accurate evaluation of $\widehat{U}_G(\mathbf{k})$.

Once $\widehat{U_G}(\mathbf{k})$ is available, the calculation of Φ consists of four steps and is summarized in the following algorithm.

2.1. Anisotropic density. In this subsection, we study the optimal zero-padding factor for the anisotropic density case, a situation that is frequently encountered in

Algorithm 1 Fast computation of Φ (2.13) by KTM.

Comment: Precompute the Fourier transform of the truncated kernel $\widehat{U_G}(\mathbf{k})$.
1: Extend the density $\rho(\mathbf{x})$ to $\mathbf{R}_{SL}$ by zero-padding.
2: Compute $\widetilde{\rho}_{\mathbf{k}}$ in (2.11) via FFT.
3: Compute $\widetilde{\rho}_{\mathbf{k}}\widehat{U_G}(\mathbf{k})$ by pointwise multiplication.
4: Compute Φ in (2.13) on mesh grid $\mathcal{T}_N$ via iFFT.

lower-dimensional confined quantum systems [5, 6]. We assume that the density is compactly supported in an anisotropic rectangle

$$\mathbf{R}_L^{\boldsymbol{\gamma}} := \prod_{j=1}^{d} [-L\gamma_j, L\gamma_j], \tag{2.16}$$

which is also domain of interest, with the anisotropy vector $\boldsymbol{\gamma} = (\gamma_1, \ldots, \gamma_d) \in \mathbb{R}^d$. Without loss of generality, we take $\gamma_1 = 1$ and $0 < \gamma_j \leq 1$ for $j = 2, \ldots, d$ and define the anisotropy strength as

$$\gamma_f := \prod_{j=1}^{d} \gamma_j^{-1}.$$

A smaller γ_j implies a shorter extend of the density $\rho(\mathbf{x})$ in the jth direction, and leads to a stronger anisotropy strength γ_f. The density is sampled on a uniform mesh grid with the same number of grid points in each spatial direction (denoted by N). Similarly to (2.3), we have

$$\Phi(\mathbf{x}) = \int_{\mathbf{B}_G} U(\mathbf{y})\rho(\mathbf{x}-\mathbf{y})\mathrm{d}\mathbf{y}, \qquad \mathbf{x} \in \mathbf{R}_L^{\boldsymbol{\gamma}}, \tag{2.17}$$

where the radius $G = 2L\sqrt{1+\gamma_2^2+\cdots+\gamma_d^2}$ is also the diameter of $\mathbf{R}_L^{\boldsymbol{\gamma}}$. To integrate (2.17), we need to approximate the density on a large domain, because for any $\mathbf{x} \in \mathbf{R}_L^{\boldsymbol{\gamma}}$ and $\mathbf{y} \in \mathbf{B}_G$ we have

$$\mathbf{x}-\mathbf{y} \in \widetilde{\mathbf{R}} := \{\mathbf{z} \in \mathbb{R}^d \;\big|\; |z_j| \leq G + L\gamma_j, j = 1, \ldots, d\}. \tag{2.18}$$

We choose to apply the Fourier spectral method on $\mathbf{R}_{L\boldsymbol{S}}^{\boldsymbol{\gamma}} := \prod_{j=1}^{d}[-S_jL\gamma_j, S_jL\gamma_j]$, where $\boldsymbol{S} = (S_1, \ldots, S_d) \in \mathbb{R}^d$ with $S_j \geq 1$ being the zero-padding factor in the jth spatial direction, so as to obtain a spectral approximation of the density on $\widetilde{\mathbf{R}}$. Similarly, once the following condition

$$G + L\gamma_j \leq (2S_j - 1)L\gamma_j \quad \Longrightarrow \quad 1 + \gamma_j^{-1}\sqrt{1+\gamma_2^2+\ldots+\gamma_d^2} \leq S_j \tag{2.19}$$

is satisfied, we derive the optimal factor as follows:

$$S_j = 1 + \gamma_j^{-1}\sqrt{1+\gamma_2^2+\ldots+\gamma_d^2}, \quad j = 1, \ldots, d. \tag{2.20}$$

The above factor will be reduced to (2.7) if the anisotropic strength is one, i.e., $\gamma_f = 1$. It is clear that the optimal zero-padding factor may be different along each spatial direction for the anisotropic density case. In practice, the optimal factor along the

jth direction is $\lceil S_j \rceil$, and the minimum memory costs are $\prod_{j=1}^{d} \lceil S_j \rceil$ times that of the original density. Take the 2D case for example, when the anisotropy strength γ_f gets stronger, we have

$$S_1 = 1 + \sqrt{1+\gamma_2^2} \approx 2 + \frac{\gamma_2^2}{2}, \quad S_2 = 1 + \gamma_2^{-1}\sqrt{1+\gamma_2^2} \approx \frac{1}{\gamma_2} + 1 + \frac{\gamma_2}{2}, \quad \gamma_2 \to 0.$$

Therefore, the minimum memory costs scale linearly with respect to the anisotropy strength as $2(1+\gamma_f)$. The stronger the anisotropy strength, the more memory storage it requires.

Similarly, after plugging in the density's Fourier series's approximation, we obtain

$$\Phi(\mathbf{x}) \approx \sum_{\mathbf{k}} \widehat{U_G}(\mathbf{k})\ \widehat{\rho}_{\mathbf{k}}\ e^{i\mathbf{k}\cdot\mathbf{x}}, \qquad \mathbf{x} \in \mathbf{R}_L^{\gamma}, \tag{2.21}$$

where $\mathbf{k} = \frac{\pi}{L}\ (\frac{k_1}{S_1\gamma_1}, \ldots, \frac{k_d}{S_d\gamma_d}), k_j = -S_jN/2, \ldots, S_jN/2 - 1$. The density's Fourier coefficients

$$\widehat{\rho}_{\mathbf{k}} = \frac{1}{|\mathbf{R}_{L\boldsymbol{S}}^{\gamma}|} \int_{\mathbf{R}_{L\boldsymbol{S}}^{\gamma}} \rho(\mathbf{z}) e^{-i\mathbf{k}\cdot\mathbf{z}} \mathrm{d}\mathbf{z},$$

are well resolved by applying the trapezoidal rule on a uniform mesh grid, and the resulting summation can be accelerated by FFT.

2.2. Tensor acceleration. As pointed out in [21], the above algorithm can be rewritten as a discrete convolution of a tensor and density grid values. The tensor T is actually the inverse discrete Fourier transform of vector $\{\widehat{U_G}(\mathbf{k}), \mathbf{k} \in \Lambda\} \in \mathbb{C}^{(SN)^d}$. With a change of index, it is easy to check that the discrete convolution structure holds true for both symmetric and nonsymmetric kernels.

To be exact, let us take the 2D case as an example. Define the index set

$$\mathcal{I}_N = \left\{(n,m) \in \mathbb{Z}^2 | -N/2 \le n \le N/2-1, -N/2 \le m \le N/2-1\right\}. \tag{2.22}$$

The Fourier transform of the density is approximated as follows,

$$\widetilde{\rho}(\mathbf{k}_{pq}) = \frac{1}{(SN)^2} \sum_{(n',m') \in \mathcal{I}_N} \rho(x_{n'}, y_{m'}) e^{-\frac{2\pi i}{SN}(pn'+qm')}, \quad \mathbf{k}_{pq} \in \Lambda, \tag{2.23}$$

and it deserves being pointed out that (n', m') belongs to $\mathcal{I}_N$ not $\mathcal{I}_{SN}$ since the density ρ is compactly supported in $\mathbf{R}_L$. Plugging (2.23) into (2.13) and switching the summation order, the discrete potential Φ on a uniform grid can be rewritten as

$$\begin{aligned}
\Phi_{n,m} &= \sum_{(p,q) \in \mathcal{I}_{SN}} \widehat{U_G}\left(\frac{\pi p}{SL}, \frac{\pi q}{SL}\right) \widetilde{\rho}(\mathbf{k}_{pq}) e^{\frac{2\pi i}{SN}(pn+qm)}, \\
&= \sum_{(n',m') \in \mathcal{I}_N} \left[\frac{1}{(SN)^2} \sum_{(p,q) \in \mathcal{I}_{SN}} \widehat{U_G}\left(\frac{\pi p}{SL}, \frac{\pi q}{SL}\right) e^{\frac{2\pi i}{SN}\left(p(n-n')+q(m-m')\right)} \right] \rho_{n',m'}.
\end{aligned}$$

Then we obtain the discrete convolution reformulation as follows,

$$\Phi_{n,m} := \sum_{(n',m') \in \mathcal{I}_N} T_{n-n',m-m'}\ \rho_{n',m'}, \qquad (n,m) \in \mathcal{I}_N, \tag{2.24}$$

where the tensor $T_{n,m}$ is given explicitly as

$$T_{n,m} = \frac{1}{(SN)^2} \sum_{(p,q)\in\mathcal{I}_{SN}} \widehat{U_G}\left(\frac{\pi p}{SL}, \frac{\pi q}{SL}\right) e^{\frac{2\pi i}{SN}(pn+qm)}, \quad (n,m)\in\mathcal{I}_{2N}, \tag{2.25}$$

and it can be computed by applying the inverse discrete Fourier transform on vector $\{\widehat{U_G}(\mathbf{k}), \mathbf{k}\in\Lambda\}$.

Following the same procedure, we derive a very similar convolution structure for the anisotropic density case. The discrete convolution tensor $T_{n,m}$ reads as follows,

$$T_{n,m} = \frac{1}{S_1 S_2 N^2} \sum_{p=-S_1N/2}^{S_1N/2-1} \sum_{q=-S_2N/2}^{S_2N/2-1} \widehat{U_G}\left(\frac{\pi p}{S_1 L\gamma_1}, \frac{\pi q}{S_2 L\gamma_2}\right) e^{\frac{2\pi i}{N}(\frac{pn}{S_1}+\frac{qm}{S_2})}, \tag{2.26}$$

and it can be computed by iFFT within $\mathcal{O}(S_1S_2N^2\log(S_1S_2N^2))$ float operations. Once the tensor $T_{n,m}$ is available, the computation of (2.24) is independent of zero-padding factor $\mathbf{S}$.

Next, we present details on how to accelerate the discrete convolution via FFT/iFFT by using the 1D example. Extension to the 2D case is quite straightforward. The convolution is given below,

$$\Phi_k = \sum_{j=-N/2}^{N/2-1} T_{k-j}\ f_j, \qquad k = -\frac{N}{2}, \ldots, \frac{N}{2}-1, \tag{2.27}$$

and with a simple index change $k\to k+(1+N/2),\ j\to j+(1+N/2)$, it is reformulated as

$$\Phi_k = \sum_{j=1}^{N} T_{k-j}\ f_j, \qquad k = 1, \ldots, N. \tag{2.28}$$

For convenience, we set $T_{-N}=0$ and the summation (2.28) remains unchanged. Then we have

$$T_j = \frac{1}{2N} \sum_{k=1}^{2N} \widehat{T}_k\ e^{\frac{i2\pi j(k-1)}{2N}}, \qquad j = -N, \ldots, N-1, \tag{2.29}$$

with

$$\widehat{T}_k = \sum_{j=-N}^{N-1} T_j\ e^{-\frac{i2\pi j(k-1)}{2N}} = \sum_{j=0}^{N-1} T_j\ e^{-\frac{i2\pi j(k-1)}{2N}} + \sum_{j=N}^{2N-1} T_{j-2N}\ e^{-\frac{i2\pi j(k-1)}{2N}}.$$

In fact, the Fourier transform vector $\widehat{T} := [\widehat{T}_1, \ldots, \widehat{T}_{2N}]$ is just the discrete FFT of vector $\widetilde{T} = [T_0, T_1, \ldots, T_{N-1}, T_{-N}, \ldots, T_{-1}]$. Substituting (2.29) into (2.28) and switching the summation order, we have

$$\begin{aligned}\Phi_k &= \sum_{j=1}^{N} \frac{1}{2N} \sum_{p=1}^{2N} \widehat{T}_p e^{\frac{2\pi i(k-j)(p-1)}{2N}} f_j = \frac{1}{2N} \sum_{p=1}^{2N} \widehat{T}_p e^{\frac{2\pi i(k-1)(p-1)}{2N}} \left[\sum_{j=1}^{N} f_j\ e^{-\frac{2\pi i(j-1)(p-1)}{2N}}\right] \\ &:= \frac{1}{2N} \sum_{p=1}^{2N} \widehat{T}_p\ \widehat{F}_p\ e^{\frac{2\pi i(k-1)(p-1)}{2N}}, \qquad k = 1, \ldots, N,\end{aligned}$$

Algorithm 2 FFT acceleration for discrete convolution Φ_k (2.28).

Comment: Given $\{T_j\}_{j=-N}^{N-1}$ and $\{f_j\}_{j=1}^{N}$.

1: Precomputation stage: set $T_{-N}=0$ and compute $\widehat{T}:=\mathrm{FFT}(\widetilde{T})$, where vector $\widetilde{T}$ is defined as $\widetilde{T}=[T_0,T_1,\ldots,T_{N-1},T_{-N},\ldots,T_{-1}]$.

2: Compute $\widehat{F}:=\mathrm{FFT}(F)$ with $F=[f_1,\ldots,f_N,0,\ldots,0]\in\mathbb{R}^{2N}$.

3: Compute $\widehat{\Phi}:=\widehat{T}\widehat{F}$ by pointwise multiplication.

4: Compute $\widetilde{\Phi}=\mathrm{iFFT}(\widehat{\Phi})$, and set $\Phi=\widetilde{\Phi}(1:N)$.

with

$$\widehat{F}_p:=\sum_{j=1}^{N} f_j\ e^{-\frac{2\pi i(j-1)(p-1)}{2N}}=\sum_{j=1}^{2N} F_j\ e^{-\frac{2\pi i(j-1)(p-1)}{2N}},\quad p=1,\ldots,2N,$$

being the discrete Fourier transform of $F=[f_1,\ldots,f_N,0,\ldots,0]\in\mathbb{R}^{2N}$. Obviously, in the last step, Φ_k can be computed by applying iFFT on $\{\widehat{T}_p\widehat{F}_p\}_{p=1}^{2N}$ within $\mathcal{O}(2N\log(2N))$ flops.

To summarize, we present a detailed step-by-step algorithm proposed in Algorithm 2 using the 1D case.

The discrete convolution can be implemented with a pair of FFT and iFFT for a zero-padded vector of length $(2N)^d$. Such an acceleration is purely algebraic because the matrix associated with FFT/iFFT happens to be eigenvectors of the discrete tensor T, and we refer the reader to [11] for more details. Once the convolution tensor is available in the precomputation step, our algorithm involves only FFT/iFFT transforms and pointwise multiplication on vectors of length $(2N)^d$, and it still holds true for the anisotropic density case no matter how strong the anisotropy is. Compared with the no-tensor-accelerated original algorithm, memory costs are reduced dramatically from $(\prod_{j=1}^{d} S_j)N^d$ to 2^dN^d, and the improvement becomes more substantial as the anisotropy strength gets stronger.

Remark 2.5. To give a vivid illustration of the improvement, let us take a 3D convolution as example. A typical double-precision computation on a 256^3 grid requires 3.4 Gb memory with the optimal threefold zero-padding, while the fourfold original algorithm requires around 8 Gb and the reduction factor is $\frac{37}{64}\approx 60\%$. With tensor acceleration, the effective memory, once the tensor is available, requires 1 Gb which is one eighth of that in the fourfold version. For anisotropic density with $\boldsymbol{\gamma}=(1,1,\gamma)$, the minimum memory costs are around $\lceil 1+\sqrt{2}/\gamma\rceil/3\times 3.4$ Gb, which are about 15 Gb when $\gamma=1/8$, and the computational cost is reduced substantially with tensor acceleration.

2.3. Error estimates. In this subsection, we shall present the error analysis for the nonlocal potential whose error originally comes from the approximation of the density function. To quantify the error estimates, we define the following norms,

$$\|\Phi-\Phi_N\|_{\infty,\mathbf{R}_L}:=\|\Phi-\Phi_N\|_{L^\infty(\mathbf{R}_L)}=\sup_{\mathbf{x}\in\mathbf{R}_L}|(\Phi-\Phi_N)(\mathbf{x})|,$$

$$\|\Phi-\Phi_N\|_{2,\mathbf{R}_L}:=\|\Phi-\Phi_N\|_{L^2(\mathbf{R}_L)}=\left(\int_{\mathbf{R}_L}|(\Phi-\Phi_N)(\mathbf{x})|^2\mathrm{d}\mathbf{x}\right)^{1/2},$$

where $\Phi_N(\mathbf{x}) = \int_{\mathbf{B}_G} U(\mathbf{y})\rho_N(\mathbf{x}-\mathbf{y})\mathrm{d}\mathbf{y}$ is the approximation of function $\Phi(\mathbf{x})$ and N is the number of grids in each spatial dimension. We define the seminorm as follows,

$$|\rho|_{m,\mathbf{R}_L} := \left(\sum_{|\boldsymbol{\alpha}|=m} \|\partial^{\boldsymbol{\alpha}}\rho\|^2_{2,\mathbf{R}_L} \right)^{1/2}$$

with $\boldsymbol{\alpha} = (\alpha_1, \ldots, \alpha_d) \in \mathbb{Z}^d$, $|\boldsymbol{\alpha}| = \sum_{i=1}^d \alpha_i$, and $\partial^{\boldsymbol{\alpha}} = \partial^{\alpha_1}_{x_1} \cdots \partial^{\alpha_d}_{x_d}$. We use $A \lesssim B$ to denote $A \le cB$ where the constant $c > 0$ is independent of the grid number N.

THEOREM 2. *For a smooth and compactly supported function $\rho(\mathbf{x})$, assuming that* $\mathrm{supp}\{\rho\} \subsetneq \mathbf{R}_L$, *the following estimates*

$$\|\partial^{\boldsymbol{\alpha}}\Phi - (\partial^{\boldsymbol{\alpha}}\Phi)_N\|_{\infty,\mathbf{R}_L} \lesssim N^{-(m-\frac{d}{2}-|\boldsymbol{\alpha}|)}\ |\rho|_{m,\mathbf{R}_L},$$
$$\|\partial^{\boldsymbol{\alpha}}\Phi - (\partial^{\boldsymbol{\alpha}}\Phi)_N\|_{2,\mathbf{R}_L} \lesssim N^{-(m-|\boldsymbol{\alpha}|)}|\rho|_{m,\mathbf{R}_L},$$

hold true for any positive integer $m > \frac{d}{2}$, where $(\partial^{\boldsymbol{\alpha}}\Phi)_N = [U * (\partial^{\boldsymbol{\alpha}}\rho_N)]$ denotes the numerical approximation of $\partial^{\boldsymbol{\alpha}}\Phi$. Especially, when $\boldsymbol{\alpha} = \mathbf{0}$, we have

$$\|\Phi - \Phi_N\|_{\infty,\mathbf{R}_L} \lesssim N^{-(m-\frac{d}{2})}|\rho|_{m,\mathbf{R}_L}, \qquad \|\Phi - \Phi_N\|_{2,\mathbf{R}_L} \lesssim N^{-m}|\rho|_{m,\mathbf{R}_L}.$$

Proof. First, we shall derive the error estimates for the density approximation. The interpolation density $\rho_N(\mathbf{x})$ is $2SL$-periodic in each spatial direction, i.e.,

$$\rho_N(\mathbf{x}) = \rho_N(\mathbf{x} + 2SL\mathbf{p}) \quad \forall\, \mathbf{x} \in \mathbb{R}^d \text{ and } \mathbf{p} \in \mathbb{Z}^d,$$

where $S = \sqrt{d}+1$ is the optimal zero-padding factor. Using periodicity, we can obtain

$$\|\rho_N\|_{\infty,\mathbf{R}_{(2\sqrt{d}+1)L}\setminus\mathbf{R}_{SL}} = \|\rho_N\|_{\infty,\mathbf{R}_{SL}\setminus\mathbf{R}_L}, \tag{2.30}$$

$$\|\rho_N\|_{2,\mathbf{R}_{(2\sqrt{d}+1)L}\setminus\mathbf{R}_{SL}} \lesssim \|\rho_N\|_{2,\mathbf{R}_{SL}\setminus\mathbf{R}_L}. \tag{2.31}$$

From a 1D/2D graphical illustration of the periodic extension (see Figure 2), one can easily check that the above estimates hold in any d dimension.

Since $\mathrm{supp}\{\rho\} \subsetneq \mathbf{R}_L$, we then derive the following estimates:

$$\|\rho - \rho_N\|_{\infty,\mathbf{R}_{(2\sqrt{d}+1)L}} = \max\{\|\rho - \rho_N\|_{\infty,\mathbf{R}_{SL}},\ \|\rho - \rho_N\|_{\infty,\mathbf{R}_{SL}\setminus\mathbf{R}_L}\} = \|\rho - \rho_N\|_{\infty,\mathbf{R}_{SL}},$$
$$\|\rho - \rho_N\|_{2,\mathbf{R}_{(2\sqrt{d}+1)L}} \lesssim \|\rho - \rho_N\|_{2,\mathbf{R}_{SL}} + \|\rho - \rho_N\|_{2,\mathbf{R}_{SL}\setminus\mathbf{R}_L} \lesssim \|\rho - \rho_N\|_{2,\mathbf{R}_{SL}}.$$

Next, we will investigate the potential case ($\boldsymbol{\alpha} = \mathbf{0}$) and define the error function as

$$e_N(\mathbf{x}) := (\Phi - \Phi_N)(\mathbf{x}), \quad \mathbf{x} \in \mathbf{R}_L.$$

To estimate the errors, we have

$$\begin{aligned}
|e_N(\mathbf{x})| &= \left| \int_{\mathbf{B}_G} U(\mathbf{y})\,(\rho - \rho_N)\,(\mathbf{x}-\mathbf{y})\mathrm{d}\mathbf{y} \right|, \\
&\le \max_{\mathbf{x}\in\mathbf{R}_L,\ \mathbf{y}\in\mathbf{B}_G} |(\rho - \rho_N)(\mathbf{x}-\mathbf{y})| \int_{\mathbf{B}_G} U(\mathbf{y})\mathrm{d}\mathbf{y}, \\
&\le \|\rho - \rho_N\|_{\infty,\mathbf{R}_{(2\sqrt{d}+1)L}} \int_{\mathbf{B}_G} U(\mathbf{y})\mathrm{d}\mathbf{y}, \\
&= \|\rho - \rho_N\|_{\infty,\mathbf{R}_{SL}} \int_{\mathbf{B}_G} U(\mathbf{y})\mathrm{d}\mathbf{y}, \qquad \mathbf{x} \in \mathbf{R}_L.
\end{aligned}$$

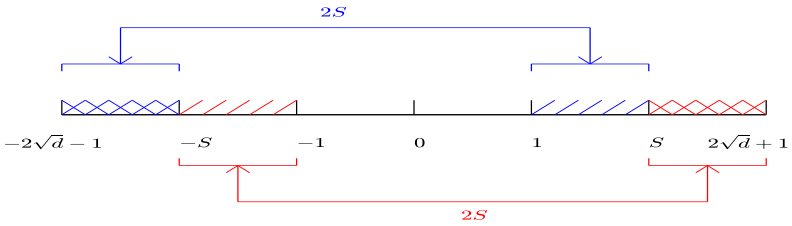

(a) The 1D schematic of periodic extension.

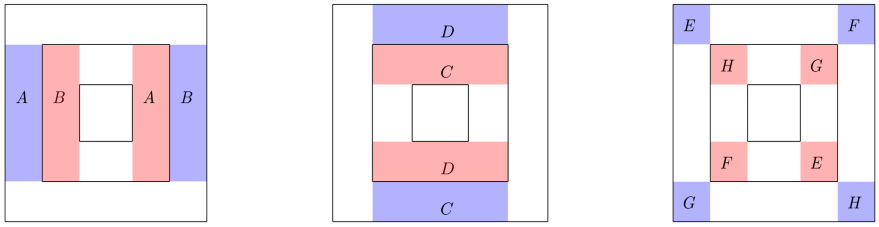

(b) The 2D schematic of periodic extension.

FIG. 2. *In 1D, the density's Fourier series approximation in* $\boldsymbol{R}_{(2\sqrt{d}+1)L} \setminus \boldsymbol{R}_{SL}$ *and* $\boldsymbol{R}_{SL} \setminus \boldsymbol{R}_{L}$ *coincide, where the period is* $2SL$ *(we take* $L = 1$ *for simplicity). In 2D, all blue regions together form* $\boldsymbol{R}_{(2\sqrt{d}+1)L} \setminus \boldsymbol{R}_{SL}$ *and all red regions belong to* $\boldsymbol{R}_{SL} \setminus \boldsymbol{R}_{L}$*. The lengths of concentric squares are* $2L$*,* $2SL$*, and* $2(2\sqrt{d}+1)L$*, respectively.*

Using Lemma 1 (see Appendix A), taking the supremum with respect to $\mathbf{x}$, we obtain

$$\|e_N\|_{\infty,\mathbf{R}_L} \lesssim \|\rho - \rho_N\|_{\infty,\mathbf{R}_{SL}} \lesssim N^{-(m-\frac{d}{2})}|\rho|_{m,\mathbf{R}_{SL}} = N^{-(m-\frac{d}{2})}|\rho|_{m,\mathbf{R}_L} \ \forall\ m > d/2.$$

As for the L^2 norm, using the Cauchy–Schwarz inequality, we obtain

$$\begin{aligned} |e_N(\mathbf{x})|^2 &= \left| \int_{\mathbf{B}_G} U(\mathbf{y}) \left(\rho - \rho_N\right)(\mathbf{x}-\mathbf{y}) \mathrm{d}\mathbf{y} \right|^2 \\ &\le \left(\int_{\mathbf{B}_G} U(\mathbf{y}) \mathrm{d}\mathbf{y} \right) \left(\int_{\mathbf{B}_G} U(\mathbf{y}) \left(\rho - \rho_N\right)^2 (\mathbf{x}-\mathbf{y}) \mathrm{d}\mathbf{y} \right). \end{aligned}$$

Integrating the above equation on both sides with respect to $\mathbf{x}$ over $\mathbf{R}_L$ and utilizing Lemma 1, we have

$$\begin{aligned} \|e_N\|_{2,\mathbf{R}_L} &\le \left(\int_{\mathbf{B}_G} U(\mathbf{y}) \mathrm{d}\mathbf{y} \right)^{1/2} \left(\int_{\mathbf{R}_L} \int_{\mathbf{B}_G} U(\mathbf{y}) \left(\rho - \rho_N\right)^2 (\mathbf{x}-\mathbf{y}) \mathrm{d}\mathbf{y}\mathrm{d}\mathbf{x} \right)^{1/2} \\ &\le \|\rho - \rho_N\|_{2,\mathbf{R}_{(2\sqrt{d}+1)L}} \left(\int_{\mathbf{B}_G} U(\mathbf{y}) \mathrm{d}\mathbf{y} \right) \\ &\lesssim \|\rho - \rho_N\|_{2,\mathbf{R}_{SL}} \lesssim N^{-m}|\rho|_{m,\mathbf{R}_{SL}} = N^{-m}|\rho|_{m,\mathbf{R}_L}. \end{aligned}$$

Last, for the general case $\boldsymbol{\alpha} \neq \mathbf{0}$, interchanging the order of convolution and differentiation, we know that

$$\partial^{\boldsymbol{\alpha}} \Phi(\mathbf{x}) = \partial^{\boldsymbol{\alpha}} (U * \rho)(\mathbf{x}) = (U * \partial^{\boldsymbol{\alpha}} \rho)(\mathbf{x}).$$

TABLE 1
A brief introduction of the examples.

Example	Content
1	3D Poisson potential
2	Comparison of KTM and GauSum (3D Poisson)
3	1D/2D Poisson potentials
4	3D/quasi-2D dipole-dipole interaction
5	2D Colomb potential
6	3D quadrupolar potential
7	Nonsmooth density

Similarly, applying results of the case $\boldsymbol{\alpha} = \mathbf{0}$ by substituting $\partial^{\boldsymbol{\alpha}}\rho$ for ρ, and combining with Lemma 1, we can complete the proof. ∎

Remark 2.6. For smooth and fast-decaying density, it is reasonable to truncate the whole space into a bounded domain such that the truncation errors are negligible; therefore, we can treat such density as a smooth and compactly supported function and apply Theorem 2. In this case, the Fourier approximation is of spectral accuracy.

Remark 2.7. For fast-decaying but nonsmooth density, the convergence rates of the potential and its derivatives are limited by the density's regularity, and we refer readers to Appendix A for more details on the Fourier approximation of a low-regularity function.

3. Numerical results. In this section, we shall investigate the effect of an optimal zero-padding factor for the nonlocal potential evaluation with isotropic and anisotropic densities, on the accuracy and efficiency for different kernels and smooth/nonsmooth density. The computational domain $\mathbf{R}_L^{\boldsymbol{\gamma}}$, where $\boldsymbol{\gamma} = (\gamma_1, \ldots, \gamma_d)$ is the anisotropy vector, is discretized uniformly in each spatial direction with mesh size h_j, and we define mesh size vector as $\mathbf{h} = (h_1, \ldots, h_d)$. For simplicity, we shall use h and $\boldsymbol{S} = (S_1, \ldots, S_d)$ to denote the mesh size if all the mesh sizes are equal, and the zero-padding vector, respectively. The algorithms were implemented in MATLAB (2016a) and run on a 3.00GH Intel(R) Xeon(R) Gold 6248R CPU with a 36 MB cache in Ubuntu GNU/Linux.

The numerical errors are measured in the following norms:

$$\mathcal{E}_\infty := \frac{\|\Phi - \Phi_{\mathbf{h}}\|_{l^\infty}}{\|\Phi\|_{l^\infty}} = \frac{\max_{\mathbf{x}\in\mathcal{T}_{\mathbf{h}}}|\Phi(\mathbf{x}) - \Phi_{\mathbf{h}}(\mathbf{x})|}{\max_{\mathbf{x}\in\mathcal{T}_{\mathbf{h}}}|\Phi(\mathbf{x})|},$$
$$\mathcal{E}_2 := \frac{\|\Phi - \Phi_{\mathbf{h}}\|_{l^2}}{\|\Phi\|_{l^2}} = \sqrt{h^d \sum_{\mathbf{x}\in\mathcal{T}_{\mathbf{h}}} |\Phi(\mathbf{x}) - \Phi_{\mathbf{h}}(\mathbf{x})|^2} \Big/ \sqrt{h^d \sum_{\mathbf{x}\in\mathcal{T}_{\mathbf{h}}} |\Phi(\mathbf{x})|^2}, \tag{3.1}$$

where $\Phi_{\mathbf{h}}$ is the numerical solution on mesh grid $\mathcal{T}_{\mathbf{h}}$ and $\Phi(\mathbf{x})$ is the exact solution.

For convenience and clarity, we present Table 1 to briefly introduce all the examples below.

3.1. Poisson potential in 1D/2D/3D.

Example 1. Here, we consider the 3D Poisson potential, i.e., we take the convolution kernel as $U(\mathbf{x}) = \frac{1}{4\pi|\mathbf{x}|}$. To this end, we take $\boldsymbol{\gamma} = (1, 1, \gamma_3)$ with $\gamma_3 \leq 1$ and consider the following two types of source density.

TABLE 2
Errors of the 3D Poisson potential for isotropic and anisotropic densities in Example 1.

	Isotropic density				
	h	2	1	1/2	1/4
$\mathcal{E}_\infty$	$S=2$	4.2908E-01	1.0283E-01	1.0276E-01	1.0276E-01
	$S=3$	4.2117E-01	2.9848E-03	1.8552E-08	3.7007E-16
	$S=4$	4.2046E-01	2.9596E-03	2.0106E-08	3.7007E-16
$\mathcal{E}_2$	$S=2$	6.6447E-01	2.8525E-01	2.8527E-01	2.8528E-01
	$S=3$	3.5839E-01	4.0630E-04	4.3402E-09	1.7989E-16
	$S=4$	3.5837E-01	4.0313E-04	4.1639E-09	1.9582E-16
	Anisotropic density				
	γ_3	1	1/2	1/4	1/8
$\mathcal{E}_\infty$	Case I	3.3307E-16	5.4171E-15	4.8932E-15	3.8102E-15
	Case II	5.1902E-16	5.6243E-15	5.3014E-15	4.1688E-15
$\mathcal{E}_2$	Case I	2.3098E-16	4.2226E-15	3.7420E-15	3.4759E-15
	Case II	3.1399E-16	3.9508E-15	3.8557E-15	3.5657E-15
	$\boldsymbol{S}$	(3, 3, 3)	(2.5, 2.5, 4)	(2.5, 2.5, 7)	(2.5, 2.5, 12.5)

- *Case* I: Isotropic (when $\gamma_3 = 1$)/anisotropic density

$$\rho(\mathbf{x}) = e^{-(x^2+y^2+z^2/\gamma_3^2)/\sigma^2} =: \rho_0(\mathbf{x}), \qquad \sigma > 0.$$

The corresponding Poisson potential could be computed analytically as [10]

$$\begin{aligned}\Phi(\mathbf{x}) =: \Phi_0(\mathbf{x}) &= U * \rho_0(\mathbf{x}) \\ &= \begin{cases} \frac{\sigma^3\sqrt{\pi}}{4|\mathbf{x}|}\mathrm{Erf}\,(\frac{|\mathbf{x}|}{\sigma}), & \gamma_3 = 1, \\ \frac{\gamma_3\sigma^2}{4}\int_0^\infty e^{-\frac{x^2+y^2}{\sigma^2(t+1)}-\frac{z^2}{\sigma^2(t+\gamma_3^2)}}/\sqrt{(t+1)^2(t+\gamma_3^2)}\,\mathrm{d}t, & \gamma_3 \neq 1, \end{cases}\end{aligned} \tag{3.2}$$

where $\mathrm{Erf}\,(x) = \frac{2}{\sqrt{\pi}}\int_0^x e^{-t^2}\mathrm{d}t$ is the error function [2].

- *Case* II: Shifted density $\rho(\mathbf{x}) = \rho_0(\mathbf{x}) + \rho_0(\mathbf{x}-\mathbf{x}_0)$. The corresponding Poisson potential analytically reads as $\Phi(\mathbf{x}) = \Phi_0(\mathbf{x}) + \Phi_0(\mathbf{x}-\mathbf{x}_0)$.

Table 2 presents errors of the 3D Poisson potential for isotropic and anisotropic densities. For the isotropic case, i.e., $\gamma_3 = 1$, we consider Case I with $L = 8, \sigma = \sqrt{1.2}$. For the anisotropic case, we consider Case I with $L = 12, \sigma = 2, \mathbf{h} = \frac{1}{2}\boldsymbol{\gamma}$ and Case II with $L = 16, \sigma = 2, \mathbf{x}_0 = (2, 2, 0)$, and $\mathbf{h} = \frac{1}{4}\boldsymbol{\gamma}$. The optimal zero-padding factor is chosen as an integer multiple of $\frac{1}{2}$, e.g., $S = 2.5 \approx \sqrt{2} + 1$. From Table 2, we can conclude that for the 3D nonlocal potential computation via KTM: (i) the twofold zero-padding is insufficient, the fourfold zero-padding is redundant, and the threefold is optimal; (ii) the optimal factor for the anisotropic density grows linearly with the anisotropy strength γ_f; (iii) the errors measured in the relative maximum norm behave similarly as those in the relative l^2 norm. Therefore, we choose to omit the errors $\mathcal{E}_2$ hereafter for brevity.

To investigate the efficiency, we present the performance of KTM with/without tensor acceleration in terms of memory costs and CPU time in Table 3, where we choose isotropic density in Case I with $L = 8, \sigma = \sqrt{1.2}$, and $h = 1/16$. The computation is split into two parts: the precomputation part(*PreComp*): computation of the tensor $\widehat{T_{\mathbf{k}}}$ or $\widehat{U_G}$ in the tensor/no-tensor version, and the execution part (*Execution*). In Figure 3, we plot the CPU times of PreComp and Execution with/without the tensor acceleration version for different anisotropy strengths γ_f.

TABLE 3
The performance of KTM for 3D Poisson potential (isotropic case) in Case I *of Example* 1.

		PreComp		Execution	
Tensor	S	Mem(Gb)	Time(s)	Mem(Gb)	Time(s)
Yes	3	4.4	59.80	2.3	19.31
	4	9.0	158.58	2.3	19.32
No	3	3.4	12.53	7.0	61.18
	4	8.0	32.96	16.3	167.00

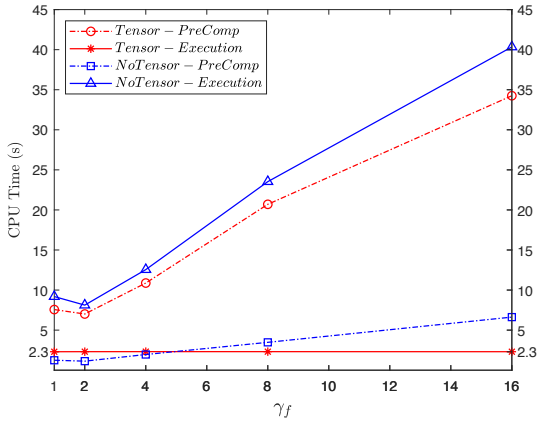

FIG. 3. *Timing results of KTM versus increasing anisotropy strength* γ_f.

From Table 3, we can see that, compared with the classical fourfold zero-padding version, KTM with an optimal factor greatly reduces the memory and computational costs, therefore, computation of a larger size is now possible on personal computers. Moreover, once the precomputation step is done, the effective computation consists of only a pair of FFT/iFFT on vectors of twice the length in each direction, no matter how strong anisotropy strength gets, and this facilitates multiple potential evaluations on the same setups. It is worth noting that the seemingly incorrect drop down at $\gamma_f = 2$ in the "Tensor-PreComp" curve is actually caused by the integer multiple of 0.5 selection in S_i. The total zero-padding factor $\prod_{i=1}^{3} S_i$ is 25 for $\gamma_f = 2$ and 27 when $\gamma_f = 1$ (the isotropic case).

Example 2. **Comparison of KTM and GauSum** [10].

Here, we consider the 3D Poisson potential with a Gaussian density $\rho(\mathbf{x}) = e^{-|\mathbf{x}|^2/\sigma^2}$, and the corresponding potential is given explicitly as an isotropic case ($\gamma_3 = 1$) in (3.2).

Table 4 presents the errors $\mathcal{E}_\infty$ and computation time for KTM and GauSum, with $\sigma = \sqrt{1.2}$ on the domain $[-8, 8]^3$. The GauSum method splits the convolution into a regular integral (I_1) and a near-field singular correction integral (I_2) [10]. T_1, T_2, and T_{total} denote hereafter the time for evaluation of I_1, I_2, and the total time, respectively. The CPU time shown in this table does not include the precomputation time, since it is usually not relevant for most applications where the nonlocal potential is evaluated many times on the same grid.

From Table 4, we can see that the execution time of KTM (T_{total}) is similar to the time T_1 in the GauSum method, because both can be implemented with a pair

TABLE 4
The performance of KTM and GauSum in Example 2 (FORTRAN language).

$N = 256^3$	$\mathcal{E}_\infty$	$T_1(s)$	$T_2(s)$	$T_{total}(s)$
KTM	5.5525E-16	-	-	14.25
GauSum	5.5547E-16	14.98	1.78	16.76

of FFT/iFFT on a zero-padded vector of length $(2N)^3$. Additionally, the remaining part, I_2, of the GauSum method can be implemented with a pair of FFT/iFFT on a vector of length N^3. Consequently, we can conclude that the efficiency of KTM is better. For the anisotropic case, we can draw a similar conclusion, since the time listed in Table 4 is independent of the anisotropy strength.

Example 3. Here, we consider the 1D and 2D Poisson potentials with convolution kernel

$$U(\mathbf{x}) = \begin{cases} -\frac{1}{2}|x|, & \text{1D Poisson,} \\ -\frac{1}{2\pi}\ln(|\mathbf{x}|), & \text{2D Poisson.} \end{cases}$$

To this end, we consider the following two cases

- Isotropic source density: we take the Gaussian $\rho(\mathbf{x}) = e^{-|\mathbf{x}|^2/\sigma^2}$. The corresponding 1D and 2D Poisson potentials could be analytically integrated as [11]

$$\Phi(\mathbf{x}) = \begin{cases} -\frac{\sigma^2}{2}e^{-x^2/\sigma^2} - \frac{\sqrt{\pi}\sigma}{2}x\,\mathrm{Erf}\,(\frac{x}{\sigma}), & \text{1D Poisson,} \\ -\frac{\sigma^2}{4}\left[E_1(\frac{|\mathbf{x}|^2}{\sigma^2}) + 2\ln(|\mathbf{x}|)\right], & \text{2D Poisson,} \end{cases}$$

  where $\sigma > 0$ and $E_1(r) := \int_r^\infty t^{-1}e^{-t}dt$ for $r > 0$ is the exponential integral function [2].
- Anisotropic source density: we take

$$\rho(\mathbf{x}) = e^{-\frac{x^2}{\sigma^2}-\frac{y^2}{\alpha^2}}\left(-\frac{4x^2}{\sigma^4} - \frac{4y^2}{\alpha^4} + \frac{2}{\alpha^2} + \frac{2}{\sigma^2}\right), \quad \sigma > 0,\ \alpha > 0.$$

  The corresponding 2D Poisson potential reads as $\Phi(\mathbf{x}) = e^{-\frac{x^2}{\sigma^2}-\frac{y^2}{\alpha^2}}$.

Table 5 presents errors of the 1D/2D Poisson potentials for isotropic and anisotropic densities. For the isotropic case, the parameters are chosen as $L = 8$, $\sigma = \sqrt{1.2}$, and we can see clearly that twofold/threefold zero-padding is optimal for the 1D/2D problems, respectively. Moreover, if a fractional zero-padding is considered, **2.5**-fold padding is more efficient for 2D problems in terms of memory costs and computation time. For the anisotropic case, the parameters are chosen as $L = 10, \sigma = 1.2, \alpha = \gamma_2\sigma, \boldsymbol{\gamma} = (1, \gamma_2)$, and $\mathbf{h} = \frac{1}{4}\boldsymbol{\gamma}$.

3.2. The 3D/quasi-2D dipole-dipole interaction (DDI).

Example 4. We consider the following two cases:
The 3D DDI: The kernel is given as

$$U(\mathbf{x}) = \frac{3}{4\pi}\frac{\mathbf{m}\cdot\mathbf{n} - 3(\mathbf{x}\cdot\mathbf{m})(\mathbf{x}\cdot\mathbf{n})/|\mathbf{x}|^2}{|\mathbf{x}|^3}, \quad \mathbf{x} \in \mathbb{R}^3,$$

where $\mathbf{n}$, $\mathbf{m} \in \mathbb{R}^3$ are unit vectors representing the dipole orientations, and the 3D potential is reformulated as [4, 5, 7, 13, 23, 24]

$$\Phi(\mathbf{x}) = -(\mathbf{m}\cdot\mathbf{n})\rho(\mathbf{x}) - 3\frac{1}{4\pi|\mathbf{x}|} * (\partial_{\mathbf{nm}}\rho),$$

TABLE 5
Errors of the 1D/2D Poisson potentials for isotropic and anisotropic densities in Example 3.

	Isotropic density				
	h	2	1	1/2	1/4
1D	$S=1$	2.1299	1.9228	1.9227	1.9227
	$S=2$	1.0356E-01	1.3938E-04	6.3941E-10	4.5744E-16
	$S=3$	1.1294E-01	2.2359E-03	1.3244E-07	6.4328E-16
2D	$S=2$	3.0583E-01	4.5718E-02	4.7154E-02	4.7154E-02
	$S=2.5$	2.0928E-01	1.4561E-03	4.8882E-08	1.6780E-15
	$S=3$	2.2027E-01	1.0051E-03	2.0456E-08	1.6780E-15
	$S=4$	2.2778E-01	1.3082E-03	7.9905E-08	1.1441E-15
	Anisotropic density				
	γ_2	1	1/2	1/4	1/8
2D	$\mathcal{E}_\infty$	5.1070E-15	5.3429E-15	1.0596E-14	3.5612E-14
	$\boldsymbol{S}$	(2.5, 2.5)	(2.5, 3.5)	(2.5, 5.5)	(2, 9.5)

where $\partial_{\mathbf{m}} = \mathbf{m}\cdot\nabla$ and $\partial_{\mathbf{nm}} = \partial_{\mathbf{n}}(\partial_{\mathbf{m}})$. In fact, the potential can be calculated via the 3D Poisson potential with source term $\partial_{\mathbf{nm}}\rho$, which can be easily computed numerically via the Fourier spectral method [20].

The quasi-2D DDI: The kernel is given as [9, 4]

$$\begin{aligned} U(\mathbf{x}) &= -\frac{3}{2}(\partial_{\mathbf{n}_\perp\mathbf{n}_\perp} - n_3^2\nabla^2)\frac{1}{(2\pi)^{3/2}}\int_{\mathbb{R}}\frac{e^{-s^2/2}}{\sqrt{|\mathbf{x}|^2+\varepsilon^2 s^2}}\mathrm{d}s \\ &:= -\frac{3}{2}(\partial_{\mathbf{n}_\perp\mathbf{n}_\perp} - n_3^2\nabla^2)\widetilde{U}(\mathbf{x}), \quad \mathbf{x}\in\mathbb{R}^2, \end{aligned}$$

where $\varepsilon > 0$, $\nabla_\perp^2 = \Delta$, $\mathbf{n}_\perp = (n_1, n_2)^T$, $\partial_{\mathbf{n}_\perp} = \mathbf{n}_\perp\cdot\nabla_\perp$, and $\partial_{\mathbf{n}_\perp\mathbf{n}_\perp} = \partial_{\mathbf{n}_\perp}(\partial_{\mathbf{n}_\perp})$, and the 2D potential can be reformulated similarly as a convolution of $\widetilde{U}$ and an effective density $\widetilde{\rho}$ as follows:

$$\Phi(\mathbf{x}) = \widetilde{U} * \left[-\frac{3}{2}(\partial_{\mathbf{n}_\perp\mathbf{n}_\perp} - n_3^2\nabla^2)\right]\rho = \widetilde{U} * \widetilde{\rho}.$$

For a Gaussian density $\rho(\mathbf{x}) = e^{-|\mathbf{x}|^2/\sigma^2}$, the DDI potentials are given explicitly as

$$\Phi(\mathbf{x}) = \begin{cases} -(\mathbf{m}\cdot\mathbf{n})\rho(\mathbf{x}) - 3\partial_{\mathbf{nm}}\left(\frac{\sigma^2\sqrt{\pi}}{4}\frac{\mathrm{Erf}\ (r/\sigma)}{r/\sigma}\right), & d=3, \\ \frac{12}{\sigma^4}e^{-\frac{r^2}{\sigma^2}}\pi\int_0^\infty \widetilde{U}(t)te^{-\frac{t^2}{\sigma^2}}[(-\sigma^2+r^2+t^2)I_0(\frac{2rt}{\sigma^2}) - 2rtI_1(\frac{2rt}{\sigma^2})]\mathrm{d}t, & d=2, \end{cases}$$

where $\mathbf{n} = (0,0,1)^T$ in the 2D case and I_0 and I_1 are the modified Bessel functions of order 0 and 1, respectively.

Table 6 shows errors of the 3D DDI (the upper part), computed with $L = 8, \sigma = \sqrt{1.2}$ with different dipole orientations $\mathbf{n} = (0.82778, 0.41505, -0.37751)^T, \mathbf{m} = (0.3118, 0.9378, -0.15214)^T$, and the quasi-2D DDI (the lower part), computed with $L = 12, \sigma = 2, \varepsilon = \frac{1}{\sqrt{32}}$, and $\mathbf{n} = (0,0,1)^T$.

3.3. The 2D Coulomb potential.

Example 5. The 2D Coulomb potential with $U(\mathbf{x}) = \frac{1}{2\pi|\mathbf{x}|}$. For anisotropic source $\rho(\mathbf{x}) = e^{-\frac{1}{\sigma^2}(x^2+\frac{y^2}{\gamma_2^2})}$ with $\gamma_2 \le 1$, the 2D Coulomb potential is given analytically as [10]

TABLE 6
Errors of the 3D DDI (upper part) and quasi-2D DDI (lower part) in Example 4.

h	2	1	1/2	1/4
$S=2$	1.5254	8.3971E-02	7.4273E-02	7.3380E-02
$S=3$	1.5763	2.9150E-02	8.4761E-07	7.0062E-15
$S=4$	1.5862	2.9422E-02	8.7784E-07	7.2865E-15
$S=2$	1.9970E-02	3.0216E-03	3.0222E-03	3.0222E-03
$S=2.5$	1.9866E-02	4.5791E-06	6.4182E-15	5.2386E-15
$S=3$	1.5975E-02	3.7262E-06	6.4768E-15	5.2042E-15
$S=4$	1.5525E-02	3.6151E-06	6.4828E-15	5.2386E-15

TABLE 7
Errors of the 2D Coulomb potential Φ and $\partial_x\Phi$ for isotropic density in Example 5.

Φ	$h=2$	$h=1$	$h=1/2$	$h=1/4$
$S=2$	2.0661E-01	2.3210E-03	1.0203E-03	1.0203E-03
$S=2.5$	2.0771E-01	2.3577E-03	2.6029E-08	4.5744E-16
$S=3$	2.0822E-01	2.2739E-03	2.7514E-08	5.7180E-16
$S=4$	2.0869E-01	2.3884E-03	2.8837E-08	3.4308E-16
$\partial_x\Phi$	$h=2$	$h=1$	$h=1/2$	$h=1/4$
$S=2$	1.0794	2.8659E-02	6.3223E-03	6.3224E-03
$S=2.5$	1.0789	2.8563E-02	1.7366E-06	8.7677E-16
$S=3$	1.0790	2.8550E-02	1.7343E-06	6.8106E-16
$S=4$	1.0791	2.8540E-02	1.7330E-06	7.3194E-16

$$\Phi(\mathbf{x}) = \begin{cases} \frac{\sqrt{\pi}\sigma}{2} I_0(\frac{|\mathbf{x}|^2}{2\sigma^2}) e^{-\frac{|\mathbf{x}|^2}{2\sigma^2}}, & \gamma_2 = 1, \\ \frac{\gamma_2\sigma}{\sqrt{\pi}} \int_0^\infty \frac{e^{-\frac{x^2}{\sigma^2(t^2+1)}} e^{-\frac{y^2}{\sigma^2(t^2+\gamma_2^2)}}}{\sqrt{t^2+1}\sqrt{t^2+\gamma_2^2}} \mathrm{d}t, & \gamma_2 \neq 1, \end{cases}$$

where $I_0(x)$ is the modified Bessel function of the first kind [2].

Table 7 shows errors of the 2D Coulomb potential Φ and its derivative $\partial_x\Phi$ for isotropic density, i.e., $\gamma_2 = 1$, $L = 8, \sigma = \sqrt{1.2}$, from which we can see clearly that the potential and its derivative can both be computed with spectral accuracy. Table 8 shows errors of the potential with anisotropic density with $L = 12, \sigma = 1.5$, and $\mathbf{h} = \frac{1}{4}(1, \gamma_2)$.

3.4. The 3D quadrupolar potential.

Example 6. The 3D quadrupole-quadrupole interaction was first proposed in [22], which reads as

$$U(\mathbf{x}) = \frac{1}{r^5} Y_4^0(\theta) = \frac{3}{16\sqrt{\pi}} \frac{1}{r^5} \left(3 - 30\cos^2\theta + 35\cos^4\theta\right), \quad \mathbf{x} \in \mathbb{R}^3,$$

where $\mathbf{x} = (x, y, z)$, $r = |\mathbf{x}|$, $\cos\theta = z/r$, and Y_4^0 is the spherical harmonic function [2]. The Fourier transform is

$$\widehat{U}(\mathbf{k}) = \frac{4\pi}{105} k^2 Y_4^0(\theta_k), \quad \mathbf{k} \in \mathbb{R}^3,$$

where $\mathbf{k} = (k_x, k_y, k_z)$, $k = |\mathbf{k}|$, and $\cos\theta_k = k_z/k$. A simple computation shows that

$$\widehat{U}(\mathbf{k}) = \frac{\sqrt{\pi}}{140}(3k^2 - 30k_z^2 + 35\frac{k_z^4}{k^2}), \tag{3.3}$$

TABLE 8
Errors of the 2D Coulomb potential for anisotropic density in Example 5.

γ_2	1	1/2	1/4	1/8	1/16
$\mathcal{E}_\infty$	5.8462E-16	2.3117E-15	1.4986E-15	1.6609E-15	2.0713E-15
$\boldsymbol{S}$	(2.5, 2.5)	(2.5, 3.5)	(2.5, 5.5)	(2, 9.5)	(2, 17.5)

TABLE 9
Errors of the 3D quadrupolar potential in Example 6.

	$h=2$	$h=1$	$h=1/2$	$h=1/4$
$S=2$	5.3856E-01	1.3009E-02	7.4579E-06	7.4579E-06
$S=3$	5.4149E-01	1.3170E-02	4.3450E-10	3.1796E-14
$S=4$	5.4252E-01	1.3227E-02	4.4095E-10	2.2994E-14

and we can clearly see that $\widehat{U}(\mathbf{k})$ is not smooth in Cartesian coordinates. Consequently, standard Fourier method results in a saturated convergence order [14]. Using partial wave expansion, we obtain the Fourier transform of the truncated kernel as follows:

$$\begin{aligned}\widehat{U_G}(\mathbf{k}) &= \int_{\mathbf{B}_G} \frac{Y_4^0(\theta)}{r^5} e^{-i\mathbf{k}\cdot\mathbf{x}} \mathrm{d}\mathbf{x} = 4\pi Y_4^0(\theta_k) \int_0^G \frac{1}{r^3} j_4(kr)\mathrm{d}r \\ &= 4\pi Y_4^0(\theta_k) \left[\frac{k^2}{105} - \frac{(-15+G^2k^2)\cos(Gk)}{G^6k^4} + \frac{3(-5+2G^2k^2)\sin(Gk)}{G^7k^5} \right].\end{aligned}$$

For a Gaussian density $\rho(\mathbf{x}) = e^{-|\mathbf{x}|^2/\sigma^2}$, the quadrupolar potential is given explicitly as

$$\begin{aligned}\Phi(\mathbf{x}) &= \frac{1}{(2\pi)^3} \int_{\mathbb{R}^3} \widehat{U}(\mathbf{k})\widehat{\rho}(\mathbf{k}) e^{i\mathbf{k}\cdot\mathbf{x}} \mathrm{d}\mathbf{k} = \frac{2}{105\pi^3} Y_4^0(\theta) \int_0^\infty k^4 \widehat{\rho}(k) j_4(kr)\mathrm{d}k \\ &= \frac{2\pi\sigma^3}{105} Y_4^0(\theta) \left[-e^{-\frac{r^2}{\sigma^2}} \left(\frac{8r^6 + 28r^4\sigma^2 + 70r^2\sigma^4 + 105\sigma^6}{r^4\sigma^7} \right) + \mathrm{Erf}\,(\frac{r}{\sigma}) \frac{105\sqrt{\pi}}{2r^5} \right].\end{aligned}$$

Table 9 presents errors of the quadrupolar potential computed with $L = 12$, $\sigma = 1.5$, zero-padding factor S, and mesh size h.

3.5. Nonsmooth density.

Example 7. We consider the 1D/2D/3D Poisson potentials and 2D Coulomb potential generated by a nonsmooth density, i.e.,

$$\rho(\mathbf{x}) = \begin{cases} \left(1 - |\mathbf{x}-\boldsymbol{\delta}|^2\right)^m, & |\mathbf{x}-\boldsymbol{\delta}| \le 1, \\ 0, & |\mathbf{x}-\boldsymbol{\delta}| > 1, \end{cases}$$

with $m \in \mathbb{Z}^+$ and $\boldsymbol{\delta} \in \mathbb{R}^d$ being the shift vector. It is clear that $\rho \in C^{m-1}(\mathbb{R}^d)$, and the corresponding nonlocal potentials are detailed explicitly in Appendix B.

Figure 4 shows the errors and convergence orders of $\partial_x\rho$ and $\partial_x\Phi$ of the Poisson potentials, where N is the grid number in each direction and $\boldsymbol{\delta} = \mathbf{0}$, $L = 2$. Figure 5 shows the errors and convergence orders of $\partial_x\Phi$ generated by the 2D Coulomb kernel with $L = 2$.

From Figures 4–5, we can see that the convergence order for $\partial_x\rho$ is $m-1$, while it is $m+1$ for $\partial_x\Phi$ in the 1D/2D/3D Poisson problems, and is m for the 2D Coulomb case. The convergence order of the potential is usually higher than that of the density, and it is compatible with Theorem 2 but performs better.

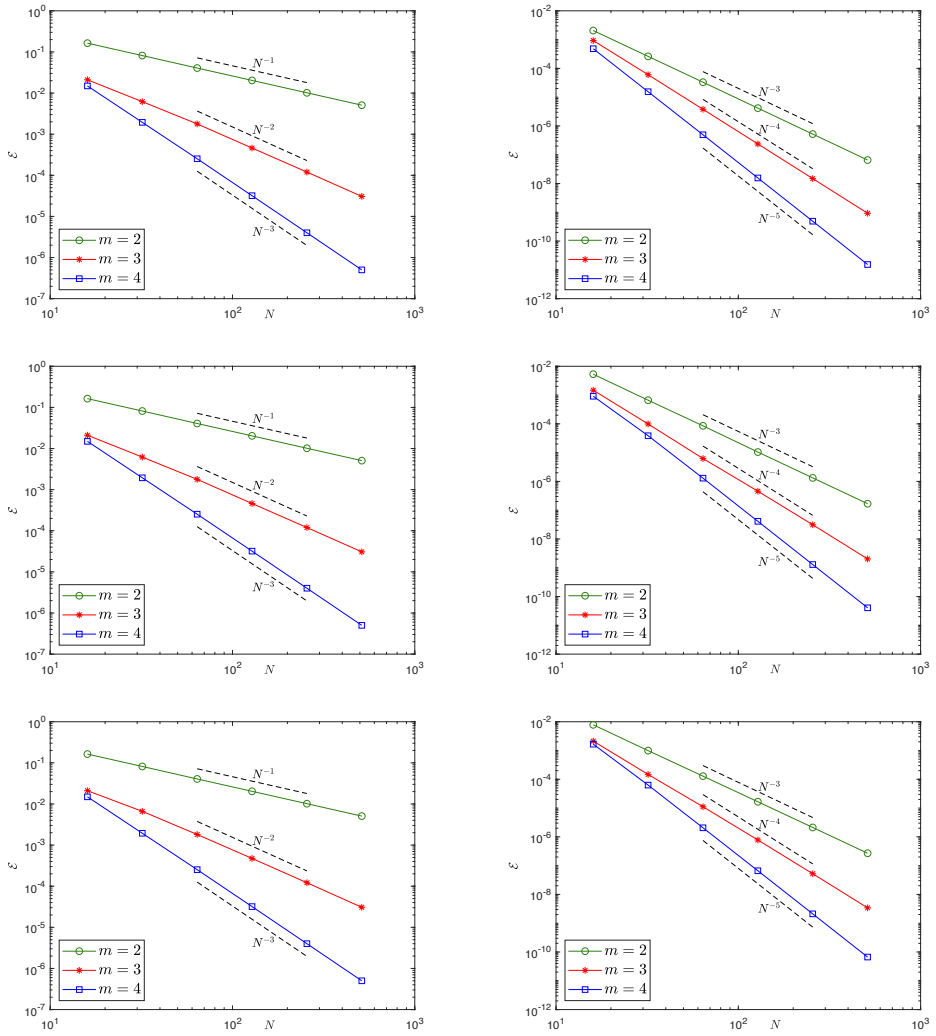

FIG. 4. *Errors of $\partial_x \rho$ (left) and $\partial_x \Phi$ (right) with $d = 1, 2, 3$ (from top to bottom) for Poisson potential with compact but nonsmooth density in* ***Example*** 7.

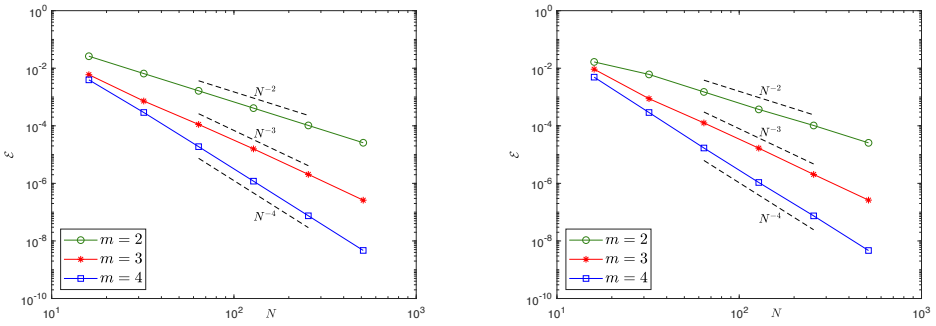

FIG. 5. *Errors of $\partial_x \Phi$ for the 2D Coulomb potential with nonsmooth density with $\boldsymbol{\delta} = (0, 0)$ (left) and $\boldsymbol{\delta} = (0.11, 0.22)$ (right) in* ***Example*** 7.

4. Conclusions. In this article, we reinvestigated the optimal zero-padding factor of the KTM in the convolution-type nonlocal potential evaluation, and strictly proved that the optimal zero-padding factor is $\sqrt{d}+1$, where d is the space dimension. The memory costs are greatly decreased to a small fraction, i.e., $(\frac{\sqrt{d}+1}{4})^d$, of that in the fourfold algorithm. We concluded that twofold padding is optimal for the 1D problem, and threefold, instead of fourfold, padding suffices to achieve spectral accuracy for the 2D and 3D problems. While for the anisotropic density, the total optimal zero-padding factor grows linearly with the anisotropy strength γ_f. The KTM is realized with the Fourier spectral method and it can be rewritten as a discrete convolution regardless of the anisotropy strength. As long as the discrete tensor is available via a precomputation step, the effective computation is merely a pair of FFT and iFFT on a double-sized density, and this is of significant importance in practical simulation, especially when the potential evaluation is called multiple times with the same setups. Rigorous error estimates were provided for both the nonlocal potential and the density in d dimension. Extensive numerical results were presented to confirm the improvement in both memory and computational costs.

Appendix A. Error estimates of Fourier spectral methods. For simplicity, we will consider 2π-periodic functions that are defined on the torus $\Omega = \mathbb{T}^d := [0, 2\pi]^d$; the extension to the general domain is quite straightforward with only minor modifications. Here we use $H_p^m(\Omega)$ to denote the 2π-periodic function space with the seminorm given below:

$$|u|_{m,\Omega} = \left(\sum_{|\boldsymbol{\alpha}|=m} \|\partial^{\boldsymbol{\alpha}} u\|_{2,\Omega}^2 \right)^{1/2} \sim \left(\sum_{\mathbf{k}\in\mathbb{Z}^d} |\mathbf{k}|^{2m} |\widehat{u}_{\mathbf{k}}|^2 \right)^{1/2}.$$

Define the Fourier and physical index sets, respectively,

$$\mathcal{I}_N := \left\{ \mathbf{k} = (k_1, \ldots, k_d) \in \mathbb{Z}^d \;\middle|\; |k_p| \le N, p = 1, \ldots, d \right\},$$
$$\mathcal{T}_N := \left\{ \mathbf{x_j} = (x_{j_1}, \ldots, x_{j_d}) \;\middle|\; x_{j_p} = j_p \pi / N, j_p = 0, \ldots, 2N-1 \right\}.$$

The Fourier interpolation series at mesh grid $\mathcal{T}_N$ reads explicitly as

$$u_N(\mathbf{x}) := \sum_{\mathbf{k}\in\mathcal{I}_N} \widetilde{u}_{\mathbf{k}}\, e^{\mathrm{i}\mathbf{k}\cdot\mathbf{x}} \text{ with } \widetilde{u}_{\mathbf{k}} = \frac{1}{(2N)^d c_{\mathbf{k}}} \sum_{\mathbf{x_j}\in\mathcal{T}_N} u(\mathbf{x_j}) e^{-\mathrm{i}\mathbf{k}\cdot\mathbf{x_j}},$$

where $c_{\mathbf{k}} := \prod_{p=1}^d c_p$ with $c_p = 1$ for $|p| < N$, and $c_p = 2$ for $|p| = N$. The error function $u - u_N$ is characterized by the following lemma, which is an extension of the 1D results in [19].

LEMMA 1. *For any $u(\mathbf{x}) \in H_p^m(\Omega)$ with $m > d/2$, we have*

$$\|\partial^{\boldsymbol{\alpha}}(u - u_N)\|_{\infty,\Omega} \lesssim N^{-(m-\frac{d}{2}-|\boldsymbol{\alpha}|)} |u|_{m,\Omega}, \quad 0 \le |\alpha| \le m,$$
$$\|\partial^{\boldsymbol{\alpha}}(u - u_N)\|_{2,\Omega} \lesssim N^{-(m-|\boldsymbol{\alpha}|)} |u|_{m,\Omega}, \quad 0 \le |\alpha| \le m.$$

Proof. Let $P_N u$ be the orthogonal projection of u, which is also named as the truncated Fourier series, i.e.,

$$(P_N u)(\mathbf{x}) = \sum_{\mathbf{k}\in\mathcal{I}_N} \widehat{u}_{\mathbf{k}} e^{\mathrm{i}\mathbf{k}\cdot\mathbf{x}} \text{ with } \widehat{u}_{\mathbf{k}} = \frac{1}{(2\pi)^d} \int_\Omega u(\mathbf{x}) e^{-\mathrm{i}\mathbf{k}\cdot\mathbf{x}} \mathrm{d}\mathbf{x}.$$

Using the Cauchy–Schwarz inequality, we obtain

$$|(P_N u - u)(\mathbf{x})| \le \sum_{\mathbf{k}\notin\mathcal{I}_N} |\hat{u}_{\mathbf{k}}| \le \sum_{|\mathbf{k}|>N} |\hat{u}_{\mathbf{k}}| \le \left(\sum_{|\mathbf{k}|>N} |\mathbf{k}|^{-2m}\right)^{1/2} \left(\sum_{|\mathbf{k}|>N} |\mathbf{k}|^{2m}|\hat{u}_{\mathbf{k}}|^2\right)^{1/2}$$

$$\lesssim \left(\int_{|\mathbf{x}|\ge N} |\mathbf{x}|^{-2m} \mathrm{d}\mathbf{x}\right)^{1/2} |u|_{m,\Omega} \lesssim N^{-(m-\frac{d}{2})}|u|_{m,\Omega}. \tag{A.1}$$

Define the interior of $\mathcal{I}_N$ as $\mathring{\mathcal{I}}_N := \left\{\mathbf{k}=(k_1,\ldots,k_d)\in\mathbb{Z}^d \;\middle|\; |k_p|<N,\ p=1,\ldots,d\right\}$ and the boundary set $\partial\mathcal{I}_N := \mathcal{I}_N \setminus \mathring{\mathcal{I}}_N$. It is clear that

$$|(P_N u - u_N)(\mathbf{x})| \le \sum_{\mathbf{k}\in\mathcal{I}_N} |\hat{u}_{\mathbf{k}} - \tilde{u}_{\mathbf{k}}| = \sum_{\mathbf{k}\in\mathring{\mathcal{I}}_N} |\hat{u}_{\mathbf{k}} - \tilde{u}_{\mathbf{k}}| + \frac{1}{c_{\mathbf{k}}} \sum_{\mathbf{k}\in\partial\mathcal{I}_N} |c_{\mathbf{k}}\hat{u}_{\mathbf{k}} - c_{\mathbf{k}}\tilde{u}_{\mathbf{k}}|$$

$$\le \sum_{\mathbf{k}\in\mathcal{I}_N} |\hat{u}_{\mathbf{k}} - c_{\mathbf{k}}\tilde{u}_{\mathbf{k}}| + \sum_{\mathbf{k}\in\partial\mathcal{I}_N} (c_{\mathbf{k}}-1)|\hat{u}_{\mathbf{k}}|. \tag{A.2}$$

The last summation is bounded and estimated as follows:

$$\sum_{\mathbf{k}\in\partial\mathcal{I}_N} (c_{\mathbf{k}}-1)|\hat{u}_{\mathbf{k}}| \lesssim \sum_{\mathbf{k}\in\partial\mathcal{I}_N} |\hat{u}_{\mathbf{k}}| \le \left(\sum_{\mathbf{k}\in\partial\mathcal{I}_N} |\mathbf{k}|^{-2m}\right)^{1/2} \left(\sum_{\mathbf{k}\in\partial\mathcal{I}_N} |\mathbf{k}|^{2m}|\hat{u}_{\mathbf{k}}|^2\right)^{1/2}$$
$$\lesssim N^{-(m-\frac{d-1}{2})}|u|_{m,\Omega}.$$

The following identity, connecting the interpolation and projection functions, holds for any function $u(\mathbf{x}) \in H_p^m(\Omega)$:

$$c_{\mathbf{k}}\tilde{u}_{\mathbf{k}} = \sum_{\mathbf{s}\in\mathbb{Z}^d} \hat{u}_{\mathbf{k}+2\mathbf{s}N}.$$

The first summation (A.2) is estimated as

$$\sum_{\mathbf{k}\in\mathcal{I}_N} |\hat{u}_{\mathbf{k}} - c_{\mathbf{k}}\tilde{u}_{\mathbf{k}}| = \sum_{\mathbf{k}\in\mathcal{I}_N} \Big|\sum_{|\mathbf{s}|>0} \hat{u}_{\mathbf{k}+2\mathbf{s}N}\Big|$$
$$\le \left(\sum_{\mathbf{k}\in\mathcal{I}_N}\sum_{|\mathbf{s}|>0} |\mathbf{k}+2\mathbf{s}N|^{-2m}\right)^{1/2} \left(\sum_{\mathbf{k}\in\mathcal{I}_N}\sum_{|\mathbf{s}|>0} |\mathbf{k}+2\mathbf{s}N|^{2m}|\hat{u}_{\mathbf{k}+2\mathbf{s}N}|^2\right)^{1/2}$$
$$\lesssim \left(\sum_{\mathbf{k}\in\mathcal{I}_N}\sum_{|\mathbf{s}|>0} |\mathbf{k}+2\mathbf{s}N|^{-2m}\right)^{1/2} |u|_{m,\Omega},$$

where the double-summation is bounded from above:

$$\sum_{\mathbf{k}\in\mathcal{I}_N}\sum_{|\mathbf{s}|>0} |\mathbf{k}+2\mathbf{s}N|^{-2m} \lesssim \sum_{\mathbf{q}\in\mathbb{Z}^d,|\mathbf{q}|\ge N} |\mathbf{q}|^{-2m} \lesssim \int_{|\mathbf{x}|\ge N-1} |\mathbf{x}|^{-2m}\mathrm{d}\mathbf{x} \lesssim N^{-(2m-d)}.$$

Then, we obtain

$$\sum_{\mathbf{k}\in\mathcal{I}_N} |\hat{u}_{\mathbf{k}} - c_{\mathbf{k}}\tilde{u}_{\mathbf{k}}| \lesssim N^{-(m-\frac{d}{2})}|u|_{m,\Omega}. \tag{A.3}$$

Combining the above estimates and applying the triangle inequality, we have

$$|(u-u_N)(\mathbf{x})| \le |(u-P_Nu)(\mathbf{x})| + |(P_Nu-u_N)(\mathbf{x})| \lesssim N^{-(m-\frac{d}{2})}|u|_{m,\Omega},$$

which, by taking the maximum norm on both sides with respect to $\mathbf{x}\in\Omega$, immediately leads to

$$\|u-u_N\|_{\infty,\Omega} = \sup_{\mathbf{x}\in\Omega}|(u-u_N)(\mathbf{x})| \lesssim N^{-(m-\frac{d}{2})}|u|_{m,\Omega}.$$

To estimate the L^2 norm, first we have

$$\|P_Nu-u\|_{2,\Omega}^2 = \sum_{\mathbf{k}\notin\mathcal{I}_N}|\hat{u}_{\mathbf{k}}|^2 \le \sum_{|\mathbf{k}|>N}|\hat{u}_{\mathbf{k}}|^2|\mathbf{k}|^{2m}|\mathbf{k}|^{-2m} \le N^{-2m}|u|_{m,\Omega}^2,$$

$$\begin{aligned}\|P_Nu-u_N\|_{2,\Omega}^2 &= \sum_{\mathbf{k}\in\mathcal{I}_N}|\hat{u}_{\mathbf{k}}-\tilde{u}_{\mathbf{k}}|^2 = \sum_{\mathbf{k}\in\mathring{\mathcal{I}}_N}|\hat{u}_{\mathbf{k}}-\tilde{u}_{\mathbf{k}}|^2 + \frac{1}{c_{\mathbf{k}}^2}\sum_{\mathbf{k}\in\partial\mathcal{I}_N}|c_{\mathbf{k}}\hat{u}_{\mathbf{k}}-c_{\mathbf{k}}\tilde{u}_{\mathbf{k}}|^2\\ &\le \sum_{\mathbf{k}\in\mathcal{I}_N}|\hat{u}_{\mathbf{k}}-c_{\mathbf{k}}\tilde{u}_{\mathbf{k}}|^2 + \sum_{\mathbf{k}\in\partial\mathcal{I}_N}(c_{\mathbf{k}}-1)^2|\hat{u}_{\mathbf{k}}|^2 \qquad \text{(A.4)}\\ &\lesssim \sum_{\mathbf{k}\in\mathcal{I}_N}|\hat{u}_{\mathbf{k}}-c_{\mathbf{k}}\tilde{u}_{\mathbf{k}}|^2 + N^{-2m}|u|_{m,\Omega}^2.\end{aligned}$$

The summation in (A.4) can be estimated by the Cauchy–Schwarz inequality as follows:

$$\begin{aligned}\sum_{\mathbf{k}\in\mathcal{I}_N}|\hat{u}_{\mathbf{k}}-c_{\mathbf{k}}\tilde{u}_{\mathbf{k}}|^2 &= \sum_{\mathbf{k}\in\mathcal{I}_N}|\sum_{|\mathbf{s}|>0}\hat{u}_{\mathbf{k}+2\mathbf{s}N}|^2\\ &\le \sum_{\mathbf{k}\in\mathcal{I}_N}\left(\sum_{|\mathbf{s}|>0}|\mathbf{k}+2\mathbf{s}N|^{-2m}\right)\left(\sum_{|\mathbf{s}|>0}|\mathbf{k}+2\mathbf{s}N|^{2m}|\hat{u}_{\mathbf{k}+2\mathbf{s}N}|^2\right)\\ &\le \max_{\mathbf{k}\in\mathcal{I}_N}\left\{\sum_{|\mathbf{s}|>0}|\mathbf{k}+2\mathbf{s}N|^{-2m}\right\}\left(\sum_{\mathbf{k}\in\mathcal{I}_N}\sum_{|\mathbf{s}|>0}|\mathbf{k}+2\mathbf{s}N|^{2m}|\hat{u}_{\mathbf{k}+2\mathbf{s}N}|^2\right)\\ &\lesssim \max_{\mathbf{k}\in\mathcal{I}_N}\left\{\sum_{|\mathbf{s}|>0}|\mathbf{k}+2\mathbf{s}N|^{-2m}\right\}|u|_{m,\Omega}^2.\end{aligned}$$

Since $|\mathbf{k}|/N \le \sqrt{d}$ holds for any $\mathbf{k}\in\mathcal{I}_N$, we have

$$\sum_{|\mathbf{s}|>0}|\mathbf{k}+2\mathbf{s}N|^{-2m} = (2N)^{-2m}\sum_{|\mathbf{s}|>0}|\mathbf{k}/2N+\mathbf{s}|^{-2m} \le CN^{-2m},$$

where the constant C is independent of N, and it can be proved using the monotonicity argument via a d-dimensional integral. It immediately suggests $\|P_Nu-u_N\|_{2,\Omega}^2 \lesssim N^{-2m}|u|_{m,\Omega}^2$. Therefore, we have

$$\|u-u_N\|_{2,\Omega} \le \|u-P_Nu\|_{2,\Omega} + \|P_Nu-u_N\|_{2,\Omega} \lesssim N^{-m}|u|_{m,\Omega}.$$

To estimate the spectral approximation error of its derivatives, following similar argument as shown above, we have

$$\begin{aligned}\|\partial^{\boldsymbol{\alpha}}(u-u_N)\|_{\infty,\Omega} &\lesssim \|\partial^{\boldsymbol{\alpha}}u - P_N(\partial^{\boldsymbol{\alpha}}u)\|_{\infty,\Omega} + \|P_N(\partial^{\boldsymbol{\alpha}}u) - \partial^{\boldsymbol{\alpha}}u_N)\|_{\infty,\Omega}\\ &\lesssim N^{-(m-\frac{d}{2}-|\boldsymbol{\alpha}|)}|u|_{m,\Omega} \qquad \text{(A.5)}\end{aligned}$$

and

$$\begin{aligned}\|\partial^{\boldsymbol{\alpha}}(u-u_N)\|_{2,\Omega} &\lesssim \|\partial^{\boldsymbol{\alpha}}u - P_N(\partial^{\boldsymbol{\alpha}}u)\|_{2,\Omega} + \|P_N(\partial^{\boldsymbol{\alpha}}u) - \partial^{\boldsymbol{\alpha}}u_N)\|_{2,\Omega}\\ &\lesssim N^{-(m-|\boldsymbol{\alpha}|)}|u|_{m,\Omega}.\end{aligned} \tag{A.6}$$

∎

Appendix B. Exact nonlocal potentials. In this appendix, we present analytical results for the Poisson/Coulomb potential generated by the following radially symmetric nonsmooth densities

$$\rho(\mathbf{x}) = \begin{cases} (1-|\mathbf{x}|^2)^m, & |\mathbf{x}| \le 1,\\ 0, & |\mathbf{x}| > 1, \end{cases} \tag{B.1}$$

where $\mathbf{x} \in \mathbb{R}^d$ and $m \in \mathbb{Z}^+$. We denote $r = |\mathbf{x}|$ and the total mass of the density by $M(\rho) := \int_{\mathbb{R}^d} \rho(\mathbf{x})\mathrm{d}\mathbf{x}$. It is clear that the corresponding potential is also radially symmetric.

The *d*-dimensional Poisson potential. The Poisson potential Φ satisfies the following equation:

$$-\Delta\Phi = \rho, \quad \mathbf{x} \in \mathbb{R}^d.$$

The potential can be derived by solving an exterior and interior Poisson problem, respectively [15]. The 3D Poisson potential reads as

$$\Phi(\mathbf{x}) = \begin{cases} c + \sum_{j=1}^{m+1} \frac{(-1)^j}{(2j)(2j+1)}\binom{m}{j-1} r^{2j}, & r \le 1,\\ M(\rho)\frac{1}{4\pi r}, & r > 1, \end{cases} \tag{B.2}$$

with $c = \frac{M(\rho)}{4\pi} + \sum_{j=1}^{m+1} \frac{(-1)^{j-1}}{(2j)(2j+1)}\binom{m}{j-1}$, while the 2D Poisson potential satisfies the following far-field boundary condition [15]

$$\lim_{|\mathbf{x}|\to\infty} \left[\Phi(\mathbf{x}) + M(\rho)\ \frac{1}{2\pi}\ln(|\mathbf{x}|)\right] = 0 \tag{B.3}$$

and we can derive the exact solution as follows,

$$\Phi(\mathbf{x}) = \begin{cases} c + \sum_{j=1}^{m+1} \frac{(-1)^j}{(2j)^2}\binom{m}{j-1}\ r^{2j}, & r \le 1,\\ -M(\rho)\frac{1}{2\pi}\ln(r), & r > 1, \end{cases} \tag{B.4}$$

where $c = \sum_{j=1}^{m+1} \frac{(-1)^{j-1}}{(2j)^2}\binom{m}{j-1}$ is determined to ensure the continuity condition at $r = 1$. The 1D Poisson potential is given explicitly as

$$\Phi(\mathbf{x}) = \begin{cases} c_1 + c_2 r + \sum_{j=1}^{m+1} \frac{(-1)^j}{(2j-1)(2j)}\binom{m}{j-1} r^{2j}, & r \le 1,\\ -M(\rho)\frac{r}{2}, & r > 1, \end{cases} \tag{B.5}$$

where $c_1 = \int_{\mathbb{R}} -\rho(x)\frac{1}{2}|x|\mathrm{d}x$ and $c_2 = -M(\rho)/2 - c_1 - \sum_{j=1}^{m+1} \frac{(-1)^j}{(2j-1)(2j)}\binom{m}{j-1} = 0$.

The 2D Coulomb potential corresponds to $U(\mathbf{x}) = \frac{1}{2\pi|\mathbf{x}|}$. For the 2D Coulomb potential, computing its Fourier integral, we obtain

$$\Phi(\mathbf{x}) = \frac{1}{2\pi}\int_0^\infty \widehat{U}(k)\widehat{\rho}(k)kJ_0(kr)\ \mathrm{d}\ k, \quad r = |\mathbf{x}|,$$

and it can be integrated exactly. Here below we just present analytic results for some fixed $m \in \mathbb{Z}^+$ and the rest can be derived using mathematical software, like Mathematica.

For $m = 2$, the 2D Coulomb potential reads as

$$\Phi(\mathbf{x}) = \begin{cases} \frac{16}{225\pi r}\left[r^2 p_0(r)E(\frac{1}{r^2}) + p_1(r)K(\frac{1}{r^2})\right], & r \le 1, \\ \frac{16}{225\pi}\left[p_0(r)E(r^2) + p_2(r)K(r^2)\right], & r > 1, \end{cases} \tag{B.6}$$

where $p_0(r) = 23 - 23r^2 + 8r^4$, $p_1(r) = 15 - 34r^2 + 27r^4 - 8r^6$, $p_2(r) = -4(2 - 3r^2 + r^4)$, and $K(r), E(r)$ are the complete elliptic integrals of first and second kind, respectively [2]. For $m = 3$, it is given explicitly as

$$\Phi(\mathbf{x}) = \begin{cases} -\frac{32}{3675\pi r}\left[r^2 l_0(r)E(\frac{1}{r^2}) + l_1(r)K(\frac{1}{r^2})\right], & r \le 1, \\ -\frac{32}{525\pi}\left[l_0(r)E(r^2) + l_2(r)K(r^2)\right], & r > 1, \end{cases} \tag{B.7}$$

with $l_0(r) = 8(-22 + 33r^2 - 23r^4 + 6r^6)$, $l_1(r) = 71 - 142r^2 + 95r^4 - 24r^6$, and $l_2(r) = -105 + 298r^2 - 353r^4 + 208r^6 - 48r^8$.

Acknowledgments. This work was done while Y. Zhang and S. Zhang were visiting Sichuan University in 2022.

REFERENCES

[1] Advanpix Multiprecision Computing Toolbox, https://www.advanpix.com.

[2] M. Abramowitz and I. A. Stegun, *Handbook of Mathematical Functions*, Dover, New York, 1965.

[3] X. Antoine, Q. Tang, and Y. Zhang, *A preconditioned conjugated gradient method for computing ground sates of rotating dipolar Bose-Einstein condensates via Kernel truncation method for dipole-dipole interaction evaluation*, Commun. Comput. Phys., 24 (2018), pp. 966–988.

[4] W. Bao and Y. Cai, *Mathematical theory and numerical methods for Bose-Einstein condensations*, Kinet. Relat. Models, 6 (2013), pp. 1–135.

[5] W. Bao, Y. Cai, and H. Wang, *Efficient numerical methods for computing ground states and dynamics of dipolar Bose-Einstein condensates*, J. Comput. Phys., 229 (2010), pp. 7874–7892.

[6] W. Bao, H. Jian, N. J. Mauser, and Y. Zhang, *Dimension reduction of the Schrödinger equation with Coulomb and anisotropic confining potentials*, SIAM J. Appl. Math., 73 (2013), pp. 2100–2123.

[7] W. Bao, Q. Tang, and Y. Zhang, *Accurate and efficient numerical methods for computing ground states and dynamics of dipolar Bose-Einstein condensates via the nonuniform FFT*, Commun. Comput. Phys., 19 (2016), pp. 1141–1166.

[8] W. Bao, S. Jiang, Q. Tang, and Y. Zhang, *Computing the ground state and dynamics of the nonlinear Schrödinger equation with nonlocal interactions via the nonuniform FFT*, J. Comput. Phys., 296 (2015), pp. 72–89.

[9] Y. Cai, M. Rosenkranz, Z. Lei, and W. Bao, *Mean-field regime of trapped dipolar Bose-Einstein condensates in one and two dimensions*, Phys. Rev. A (3), 82 (2010), 043623.

[10] L. Exl, N. J. Mauser, and Y. Zhang, *Accurate and efficient computation of nonlocal potentials based on Gaussian-sum approximation*, J. Comput. Phys., 327 (2016), pp. 629–642.

[11] L. Greengard, S. Jiang, and Y. Zhang, *The anisotropic truncated kernel method for convolution with free-space Green's functions*, SIAM J. Sci. Comput., 40 (2018), pp. A3733–A3754.

[12] M. R. Jarvis, I. D. White, R. W. Godby, and M. C. Payne, *Supercell technique for total-energy calculations of finite charged and polar systems*, Phys. Rev. B (3), 56 (1997), pp. 14972–14978.

[13] S. Jiang, L. Greengard, and W. Bao, *Fast and accurate evaluation of nonlocal Coulomb and dipole-dipole interactions via the nonuniform FFT*, SIAM J. Sci. Comput., 36 (2014), pp. B777–B794.

[14] X. Liu, Q. Tang, and Y. Zhang, *Numerical Study of the Quasi-2d Dipolar Bose-Einstein Condensates*, manuscript.

[15] N. J. Mauser and Y. Zhang, *Exact artificial boundary condition for the Poisson equation in the simulation of the 2D Schrödinger-Poisson system*, Commun. Comput. Phys., 16 (2014), pp. 764–780.
[16] S. Ronen, D. C. Bortolotti, and J. Bohn, *Bogoliubov modes of a dipolar condensate in a cylindrical trap*, Phys. Rev. A (3), 74 (2006), 012623.
[17] C. A. Rozzi, D. Varsano, A. Marini, E. K. U. Gross, and A. Rubio, *Exact Coulomb cutoff technique for supercell calculations*, Phys. Rev. B (3), 73 (2006), 205119.
[18] W. Rudin, *Functional Analysis*, 2nd ed., McGraw-Hill, New York, 1991.
[19] J. Shen, T. Tang, and L. Wang, *Spectral Methods: Algorithms, Analysis and Applications*, Springer, Berlin, 2011.
[20] L. N. Trefethen, *Spectral Methods in MATLAB*, Software Environ. Tools, SIAM, Philadelphia, 2000.
[21] F. Vico, L. Greengard, and M. Ferrando, *Fast convolution with free-space Green's functions*, J. Comput. Phys., 323 (2016), pp. 191–203.
[22] A. B. Wang and S. Yi, *Trapped Bose-Einstein condensates with quadrupole-quadrupole interaction*, Chinese Phys. B, 27 (2018), 120307.
[23] S. Yi and L. You, *Trapped atomic condensates with anisotropic interactions*, Phys. Rev. A (3), 61 (2000), 041604.
[24] S. Yi and L. You, *Trapped condensates of atoms with dipole interactions*, Phys. Rev. A (3), 63 (2001), 053607.